

# Preliminary Defense Draft

Cristilyn Gardner

Spring 2021

## Contents

<b>1</b>	<b>The Field of Exoplanets</b>	<b>1</b>
1.1	First Discoveries . . . . .	1
1.2	Previous and Current Studies/Missions . . . . .	3
1.2.1	Space-Based . . . . .	3
1.2.2	Ground-Based . . . . .	4
1.3	Future Missions . . . . .	5
1.3.1	Space-Based . . . . .	5
1.3.2	Ground-Based . . . . .	6
<b>2</b>	<b>Exoplanet Detection</b>	<b>6</b>
2.1	Detection Methods . . . . .	6
2.1.1	Transits . . . . .	6
2.1.2	Radial Velocity . . . . .	8
2.1.3	Microlensing . . . . .	9
2.1.4	Imaging . . . . .	9
2.1.5	Timing Variations . . . . .	10
2.2	Exoplanet Demographics . . . . .	10
<b>3</b>	<b>Characterizing Exoplanets via Transits</b>	<b>11</b>
3.1	Orbital Elements . . . . .	11
3.2	Basic Equations . . . . .	12
3.2.1	Eclipse Geometry . . . . .	12
3.2.2	Geometric Transit Probability . . . . .	14
3.2.3	Flux Variations During Eclipses . . . . .	14
3.2.4	Characterizing the System . . . . .	15
3.2.5	Characterizing the Atmosphere . . . . .	15
3.2.6	Limb Darkening . . . . .	16
3.3	Stellar Activity . . . . .	18
3.4	Exoplanet Modeling . . . . .	18
3.5	Hot Jupiters . . . . .	18
3.5.1	Origin Theories . . . . .	19
3.5.2	Internal Structure . . . . .	20
3.5.3	Atmospheric Properties . . . . .	21
<b>4</b>	<b>Thesis Proposal</b>	<b>25</b>
4.1	Scope of Work . . . . .	25
4.2	Photometric Requirements . . . . .	26
4.2.1	Signal to Noise Calculations . . . . .	27
<b>5</b>	<b>Appendix</b>	<b>30</b>

## 1 The Field of Exoplanets

### 1.1 First Discoveries

In 1992, Aleksander Wolszczan and Dale Frail discovered the first exoplanets with the Aricebo Radio Telescope in arguably one of the most surprising places; around a pulsar (Wolszczan and Frail, 1992). Pulsars are highly magnetized stars that emit pulses of radiation at intervals from seconds to milliseconds. Wolszczan and

Frail carefully measured the pulses coming from the 6.2 millisecond pulsar PSR1257+12 and found that the timing variations they were observing were the result of two orbiting rocky planets. In 1995, Didier Queloz and Michel Mayor discovered the first exoplanet around the Sun-type star, 51 Pegasi, using radial velocity measurements (Mayor and Queloz, 1995) with the ELODIE spectrograph. The orbiting planet is separated 0.05 AU from its host star - well inside the orbit of Mercury - with minimum mass of 0.5  $M_J$  (Jupiter mass) and short period of 4.23 days. At this point astronomers were both perplexed and intrigued at the remarkable diversity of possible planetary evolution sites revealed in these discoveries.

Two independent research teams lead by David Charbonneau and Greg Henry share the discovery of the first transiting planet, HD 209458b (Charbonneau et al., 2000; Henry et al., 2000). This was a major achievement as transiting planets allow for the analysis of the planets atmosphere. The transit provided constraints on the planetary radius and the additional radial velocity measurements (Henry et al., 2000; Mazeh et al., 2000) allowed for minimum mass measurements. Together, the mass and radius gave an estimation of the density of HD 209458b. The density of a planet is important as it has major implications for its composition.

The first planet orbiting in the ‘habitable zone’ was found by Santos et al. (2001). This is the region around a star in which the temperature just right for there to be water in its liquid form on the surface of the planet. Exo-biologists are particularly interested in this region as this could be an excellent place to search for alien life. Although HD 28185b orbits at 1 AU around a Sun-type middle-aged dwarf it in no way resembles Earth. At a minimum mass of 5.7  $M_J$ , it is a giant, gaseous planet. That same year, teams lead by David Charbonneau and Timothy Brown published the results of the first atmospheric studies of a transiting exoplanet using the *Hubble* space Telescope’s spectrograph (Charbonneau et al., 2002; Brown et al., 2001). This groundbreaking study detected sodium absorption features in the atmosphere of the now dubbed ‘hot Jupiter’ (HJ) HD 209458b (Charbonneau et al., 2002). Subsequent studies have found oxygen and carbon molecules in the HD 209458b atmosphere (e.g., Vidal-Madjar et al., 2004).

The first observation of light emanating from a planet itself was done by a team lead by Johnathan Fortney in 2005 using *Spitzer* (Fortney et al., 2005). Observing infrared light from HJ’s TrES-1b and HD 209458b allowed the orbits, sizes and atmospheres of planets to be analysed. A few years later, groups lead by Jeremy Richardson (HD 209458b Richardson et al., 2007) and Carl Grillmair (HD 189733b Grillmair et al., 2007) used *Spitzer* make the first observations of an exoplanet’s spectrum. Around the same time, Heather Knutson and David Charbonneau produced the first rough map of the temperature of cloud cover of an exoplanet – the HJ HD 189733b (Knutson et al., 2007a). They also used *Spitzer* to investigate whether the planet’s atmosphere has the ability to transport the energy from the day-side to the night-side, which determines the temperature at different points on surface of the planet.

At this point in our timeline there were only a small number of known exoplanets. It was not until the launch of NASA’s *Kepler* satellite, in 2009, that the exoplanetary field really started to gain traction. *Kepler*’s original mission was to stare at a patch of sky containing about 150,000 stars for four years and look for dips in the star’s light, signalling the possibility of a transiting exoplanet. This length of time is critical to detecting multiple transits of long-period exoplanets. Kepler 10b, the first exoplanet found by *Kepler* in 2011, is 1.4 times the size of Earth and orbits its star a staggering 20 times closer than Mercury does to the Sun. A few years later, in 2014, *Kepler* found its first Earth-sized planet, Kepler 186f, in the habitable zone. Earth’s bigger, older cousin was found in 2015. The ‘super-Earth’ Kepler 452b orbits a G-2 star and is 1.6 times the size of Earth. By the middle of 2016 Kepler had released a cache of just over 1,200 planets, with an estimated 40% of them being rocky and Earth-like in composition. The frequency at which planets were being found around the stars in the *Kepler* field was an exciting revelation. This, of course, was the point of *Kepler*; to see just how common exoplanets are in our galaxy. It turns out that exoplanets are very common! Even our closest neighbor (4.2 light-years), Proxima Centauri, hosts a planet orbiting within its habitable zone.

Campaigns like *Kepler* and TRAPPIST revealed the existence of intricate multi-planet systems. The TRAPPIST-1 system became infamous (de Wit et al., 2016) when it found seven Earth-like planets (some in the habitable zone) orbiting around a red dwarf star. Studies are currently examining these exoplanets for potential signs of life. Kepler 90 was found shortly after with eight orbiting exoplanets. This system now ties our Solar System with the most planets found around a star to date (Shallue and Vanderburg, 2018). The eight planet, Kepler 90i, was not found via the traditional methods but was discovered by using machine learning (Shallue & Vanderberg 2011). The designations of b, c, d, e, f, g and i are derived from the order in which the planet is discovered around the system.

May 2018 saw the first and long anticipated detection of helium in an exoplanet. One of the *Hubble*’s spectrographs was responsible for this detection in the atmosphere around the warm super-Neptune WASP 107b (Deming, 2018). The discovery of water vapor in the atmosphere around exoplanet K2 18b made headlines all around the globe (Cloutier et al., 2017). Interestingly, in hot, gaseous planets water vapor has now been found to be second most abundant molecular species (hydrogen being the first). K2 18b is a super-Earth and so it is relatively small, cold, and terrestrial. These characteristics make it extremely difficult to observe the atmosphere. Thus, up until this point atmospheric signatures from an exoplanet similar to K2 18 b had not yet been observed. This discovery was a ground-breaking moment for the field of exoplanetary science and

astrobiology.

The *Kepler* spacecraft had been the workhorse of exoplanet detection and in preparation for its retire, the Transiting Exoplanet Survey Satellite (*TESS*) was positioned to take its place. *TESS* is an all-sky survey that is now monitoring over 500,000 nearby stars for brightness dips. Observing the closest, brightest stars gives the best chance for studying transiting planets in depth. The *TESS* science team is expecting to find thousands of new exoplanets varying in size and orbiting around a variety of different star-types over the course of its lifetime. **As of 05/2021 there are 4,383 confirmed planets**, with 125 from *TESS* and an additional 2,684 *TESS* project candidates (Akeson et al., 2013).<sup>1</sup>

This list of firsts is expected to increase as the highly sensitive new generation of space telescopes, such as *JWST*, come online. It's fun to contemplate what wonders lay out there just waiting to be uncovered. One thing is certain, it sure is an exciting time for this field!

## 1.2 Previous and Current Studies/Missions

Here I summarize past, present, and future missions that have played or will play a significant role in contributing to the rapidly expanding exoplanetary field.

### 1.2.1 Space-Based

#### Kepler & K2

NASA's *Kepler* Space Telescope<sup>2</sup> (Borucki et al., 2010), named after famous astronomer Johannes Kepler, was launched in 2009 and sent into an Earth-trailing Heliocentric orbit. It surveyed approximately 530,506 stars over the course of its nine and a half years of operation to search for Earth-sized planets around Sun-type stars and determine their frequency in the Milky Way. This primary goal proved to be an insurmountable challenge due to the combination of the unexpectedly large noise from Sun-type stars and multiple issues with the craft's hardware. The only science instrument on board is a visual band photometer ( $\lambda = 430\text{--}890\text{ nm}$ ) that utilized its 0.95m primary mirror to monitor the brightness of these stars to look for periodic dips that signaled transiting planets. To monitor the same stars without interference, *Kepler* turned its field of view out of the ecliptic plane and to an area with the highest density of stars - the Cygnus and Lyra constellations. Its original mission was to survey approximately 150,000 main sequence stars over the course of four years. In 2013, just after finishing this four year period, two of the four reaction wheels that control the telescope's pointing failed and the original mission ended. In response to this failure, the K2 mission continued on with observations in 2014. *Kepler* sadly retired in October 2018 but not after having found a total of 2,662 exoplanets. The *Kepler* legacy is rich in discoveries and has provided an invaluable data set.

#### CoRoT

Lead by the French Space Agency (CNES) and the European Space Agency, (ESA) The Convection, Rotation and planetary Transits (*CoRoT*) Space Telescope<sup>3</sup> was launched in December 2006. Its primary mission was to make continuous observations of Milky Way star fields for up to six months at a time, looking for star vibrations (stellar seismology) and exoplanets. Making observations from 900km above Earth in the visual bands, *CoRoT* was able to find a couple hundred exoplanet candidates in about 160,000 lightcurves over its roughly seven and a half year life. Of those candidates, 34 of them have been confirmed and vigorously studied. Its science instrument was a wide field camera and an afocal telescope with a 27 cm lens. June 2014 *CoRoT* was decommissioned and sent to perish in Earth's atmosphere.

#### Spitzer

The *Spitzer* Space Telescope<sup>4</sup> was NASA's third infrared space telescope, with its three science instruments operating in the 3.6–160  $\mu\text{m}$  wavelength regime. Launched in 2003 and retiring in 2020, it had an incredible 17 year run. *Spitzer* was the first telescope with the ability to directly detect light from exoplanets, making determining characteristics such as temperature, atmospheric conditions, and winds possible. This can be done in two steps. The first is collecting the total infrared light from both the exoplanet and star when they are both visible. The second is then observing the system when the exoplanet is passing behind the star, thus collecting just the light from the star.

#### Hubble Space Telescope

Known for its breathtaking images, the *Hubble* Space Telescope<sup>5</sup>, named after astronomer Edwin Hubble, was launched by NASA in 1990 and still remains in low-Earth orbit as of today. It has a 2.4m primary mirror

<sup>1</sup>NASA Exoplanet Archive: <https://exoplanetarchive.ipac.caltech.edu>

<sup>2</sup>[https://www.nasa.gov/mission\\_pages/kepler/main/index.html](https://www.nasa.gov/mission_pages/kepler/main/index.html)

<sup>3</sup><https://corot.cnes.fr/en/COROT/index.htm>

<sup>4</sup><http://www.spitzer.caltech.edu>

<sup>5</sup><https://hubblesite.org>

that is accompanied by multiple science instruments that observe in the ultra-violet, visible, and infrared. Although *Hubble* is not primarily used to detect exoplanets, it plays a pivotal role in more probing follow-up observations. Being clear of Earth’s atmosphere gives *Hubble* particularly good seeing. Among its many firsts, *Hubble* was the first telescope to image an exoplanet directly in visible light. Its high contrast has helped astronomers infer the existence debris disks around stars including HD 141569, TW Hydrae and Beta Pictoris. To this day *Hubble* continues to make significant contributions to the field of exoplanets.

### Transiting Exoplanet Survey Satellite

The successor to *Kepler* is NASA’s Transiting Exoplanet Survey Satellite<sup>6</sup> (*TESS*) (Ricker et al., 2014). Launched in April 2018, *TESS* was designed to scan the entire sky and monitor bright, nearby stars for transiting exoplanets. Bright host stars are ideal for enabling detailed characterization of the star (e.g., temperature, metallicity, age, mass) which ultimately helps to constrain planetary parameters. Its primary, two year mission was completed by July 2020 and it is now in an extended mission. *TESS* is finding a wide variety of exoplanets; from small rocky worlds to large gas giants. Every four months the *TESS* science team provides public data releases so that the community can study the newly found planets.

### CHaracterising ExOPlanet Satellite

The ESA’s The CHaracterizing ExOPlanet Satellite (*CHEOPS*)<sup>7</sup> was launched in December 2019 and is currently performing high precision transit photometry on bright exoplanet host stars. The 32cm telescope sends the light to a photometer that is sensitive in the 330-1100 nm regime. Its primary goal is to obtain precise radii measurements on exoplanets that already have mass estimates from spectroscopic ground based surveys. Knowing the mass and radius together allows for density calculation which can help discern the exoplanets composition. What makes *CHEOPS* unique is that it is especially suited to detect shallow transits — transits of exoplanets in the Neptune to Super-Earth mass range (1–6  $R_E$ ). The precision is limited by stellar photon noise at 150 parts per million (ppm) for a star of 9<sup>th</sup> magnitude.

#### 1.2.2 Ground-Based

##### Kilodegree Extremely Little Telescope

Two small robotic telescopes, with apertures of only 4.2cm, makes up the recently decommissioned (2020) Kilodegree Extremely Little Telescope<sup>8</sup> (*KELT*) network. *KELT*-North (operational in 2008) resides in Arizona and *KELT*-South is near Sutherland, South Africa (operational in 2008). They performed a transit survey around bright host stars in the range of  $8 < V < 10$  magnitude. Radial velocity programs have extensively surveyed stars brighter than this and typical transit surveys observe stars a bit fainter than this regime. As of 2018, *KELT* discovered 22 transiting HJs (Pepper et al., 2018).

##### Wide Angle Search for Planets

Out of all of the ground-based transit finding surveys, the Wide Angle Search for Planets<sup>9</sup> (*WASP*) is currently the most successful (Street et al., 2003). At just over 150 planets found, *WASP* has played a pivotal role in finding exoplanets around bright enough stars for extensive follow-up observations. The Northern hemisphere SuperWASP site is in La Palma which is in the Canary Islands and the southern hemisphere has *WASP*-South in Sutherland, South Africa. Each site has eight small Canon cameras in an array that covers 480 degrees of sky in one exposure and takes an image every minute. Since 2006 both sites have imaged 30 million stars about 430 million times.

##### Hungarian Automated Telescope Network

The Hungarian-made Automated Telescope Network (*HATNet*) Exoplanet Survey<sup>10</sup> began in 2003 and is a network of seven small telescopes that are used to discover planets via the transit method. *HATNet* is responsible for finding 134 exoplanets to date. Like *WASP*, *HATNet* has both a Northern and Southern hemisphere component. *HATNet*-South is spread over Australia, South America and Africa and is responsible for finding 73 exoplanets.

##### Trans-Atlantic Exoplanet Survey

Beginning in 2003, three 10cm telescopes in Spain, California and Arizona made up the Trans-Atlantic Exoplanet Survey (*TrES*) (Alonso et al., 2007). When it was in use, it utilized the ability of relatively small telescopes to monitor stars and look for exoplanets via periodic dips in brightness. *TrES* was responsible for

---

<sup>6</sup><https://exoplanets.nasa.gov/tess/>

<sup>7</sup><https://cheops.unibe.ch>

<sup>8</sup><https://astronomy.osu.edu>

<sup>9</sup><https://wasp-planets.net>

<sup>10</sup><https://hatnet.org>

the discovery on five new exoplanets.

### Optical Gravitational Lensing Experiment

Running from 1992 to the present, The Optical Gravitational Lensing Experiment<sup>11</sup> (*OGLE*) has been conducting a long term variability survey (Udalski et al., 1992). Its primary goal is to find and classify variable stars, detect microlensing events, discover dwarf novae, and study the large scale structure of the Magellanic clouds and Milky Way. Since its inception, *OGLE* has found 17 exoplanets – including 6 found via the gravitational microlensing experiment and 8 with the transit method.

### XO

The *XO* Telescope (McCullough et al., 2005) sits at 3,054m in elevation at the summit of Haleakala on Maui, Hawaii. In operation since 2003, the two 200mm telephoto camera lenses have been monitoring the skies to look for exoplanets using the transit method. Its first goal was to find HJ exoplanets transiting bright stars with the use of differential photometry. Thus far it has found five HJs and one potential brown dwarf.

### Next-Generation Transit Survey

The Next-Generation Transit Survey<sup>12</sup> (*NGTS*) is specifically designed to find and characterize Neptune-sized and smaller exoplanets transiting bright ( $V < 13$  magnitude) host stars (West et al., 2016). This wide field photometric survey uses an array of small telescopes that operate in the 520–890nm optical wavelength regime. This range of wavelengths works well for early M and K spectral type stars as these types are known to be small and relatively cool. Their photometric precision is stated to be 150 ppm. This remarkable precision from the ground has led to the discovery of an exoplanet of 3 Earth radii, NGTS 4b (West et al., 2019).

### TRAnsiting Planets and Planetesimals Small Telescope

The Transiting Planets and Planetesimals Small Telescope<sup>13</sup> (*TRAPPIST*) is a pair of telescopes that use high precision differential photometry to detect and characterize transiting exoplanets. TRAPPIST-South is located in the Chilean Mountains at the La Silla Observatory and began its observations in 2010. In 2016, TRAPPIST-North started operations in Morocco. The *TRAPPIST* telescopes can detect exoplanets orbiting red dwarfs that are as small as Earth.

## 1.3 Future Missions

### 1.3.1 Space-Based

#### James Webb Space Telescope

Set to be launched in 2021, the James Webb Space Telescope<sup>14</sup> (*JWST*) is a large infrared telescope that will be succeeding Hubble as the premier space observatory in the near future. Its 6.5m primary mirror will allow for in depth study of the many phases of our universe’s history. One of its key goals is to study planetary systems and the origin of life. *JWST* will have four instruments on board including cameras and spectrometers that are capable of detecting very small signals. Unlike Hubble, which measures light in the visible and ultraviolet, *JWST* is sensitive to infrared light (0.6–28 $\mu$ m). This capability will allow the spacecraft to perform a wide range of astronomical and cosmological investigations. Most observations of exoplanets are indirect because it is difficult to image planets directly. Exoplanet host stars are usually much brighter than their planets are, and this complicates detecting light coming directly from the exoplanet itself. These instruments block the glare of the host star so that the exoplanet’s light can be observed. *JWST* has on-board coronagraphs that will allow it to take these direct images.

#### PLANetary Transits and Oscillations

The ESA’s PLANetary Transits and Oscillations of stars<sup>15</sup> (*PLATO*) primary mission is to detect and study exoplanets that are Earth-like and near the habitable zone of stars that are yellow dwarfs, sub giants, and red dwarf stars. *PLATO* will be able to determine the host stars age by precisely characterizing the star through seismic activity. It is set to be launched in 2026.

#### Nancy Grace Roman Space Telescope

In NASA’s Decadal Survey, the Nancy Grace Roman Space Telescope<sup>16</sup> (*Roman*) is rated at the top of the list of large space missions to follow *JWST*. This telescope is designed to study infrared astrophysics,

---

<sup>11</sup><http://ogle.astrouw.edu.pl>

<sup>12</sup><https://ngtransits.org>

<sup>13</sup><https://www.trappist.uliege.be>

<sup>14</sup><https://jwst.nasa.gov>

<sup>15</sup><https://sci.esa.int/web/plato>

<sup>16</sup><https://roman.gsfc.nasa.gov>

dark energy and exoplanets. Its size is comparable to *Hubble*, with its primary mirror also being 2.4m, but its field of view is nearly 100 times greater. Its two on-board instruments are the coronagraph and the wide field camera. Over the course of its 5 year mission it is estimated to find about 2,600 exoplanets via its microlensing survey. The coronagraph will be used to study nearby exoplanets in great detail. *Roman* is set to launch in the mid-2020s.

### 1.3.2 Ground-Based

#### Giant Magellan Telescope

With a primary diameter equivalent to 24.5m and a resolving power expected to be 10 times greater than *Hubble*, the Giant Magellan Telescope<sup>17</sup> (*GMT*) will be observing in the optical to near infrared part of the spectrum (320–25,000nm). The GMT-Consortium Large Earth Finder, or G-CLEF, is the first instrument planned for *GMT* and it will be used to detect Earth-mass exoplanets around Sun-type stars via extreme precision radial velocity measurements. Adaptive optics on the *GMT* will allow for images an order of magnitude sharper than *Hubble*. *GMT* is currently being built in the Las Campanas Observatory in Chile and is expected to be completed in 2029.

#### The Thirty Meter Telescope

The controversial Thirty Meter Telescope<sup>18</sup> (*TMT*) is expected to be completed and commissioned by 2027. Located on Maunakea in Hawaii, *TMT* will allow us to study deep into space with incredible sensitivity. Its resolution is expected to be 12 times sharper than seen with *Hubble*. The size and range of wavelengths available for observation will aid in the exploration of planet formation processes and exoplanet characterization.

#### Extremely Large Telescope

Coming in at a whopping 39.3m, the Extremely Large Telescope<sup>19</sup> (*ELT*) will be the biggest near infrared/optical telescope in the world. At this size *ELT* will be capable gathering almost 13 times more light than any existing optical telescope. Amongst many other things, the *ELT* will study exoplanets in exquisite detail. Its precision will allow for detection of organic molecules and water in protoplanetary disks. The *ELT* is currently being built on top of Cerro Armazones in the Atacama Desert of northern Chile and is expected to be completed in 2025.

## 2 Exoplanet Detection

Planets begin forming around a young star's gaseous disk yet the exact physical mechanisms driving the formation and evolution of planets is not well understood (Ford, 2014). This early disk can last several million years and while in them planets can grow and migrate due to an exchanges in angular momentum (Kley and Nelson, 2012). The fate of the planet inevitably varies depending on the particular circumstances. Some will migrate inward and eventually be engulfed by the host star while others will accrete dust and gaseous material from the disk they are embedded in and wind up in a location far from where they began. To gain a better understanding of these driving processes it is imperative that the discovery and study of exoplanets be a top priority in the exoplanet community. Many techniques have been implemented and are continually refined to do just that.

### 2.1 Detection Methods

There are many creative techniques available to detect exoplanets. Figure 1 shows the cumulative detections per year for each major detection method. Notice that the bulk of the detections began with the radial velocity (RV) method but then shifted dramatically to the transit method near 2014 thanks to large transit surveys.

#### 2.1.1 Transits

A planet passing in front of and behind its host star will create a periodic decrease or increase in the observed flux depending on its orbital position. Figure 2 illustrates a transiting planet's orbital path with geometry of the system and the resulting lightcurve at each point in its orbit. A *lightcurve* is a plot of the flux as a function of time and encoded within it is information about both the planet and its host star. Immediately before and after the primary transit it is the star and the planet night-side that contribute to the total flux. During the primary transit the total flux is the stellar flux minus what is blocked by the planet shadow. As the planet continues on its path behind the star its day-side becomes increasingly illuminated and thus the total flux

---

<sup>17</sup><https://www.gmto.org>

<sup>18</sup><https://www.tmt.org>

<sup>19</sup><https://www.eso.org/sci/facilities/eelt/>

## Cumulative Detections Per Year

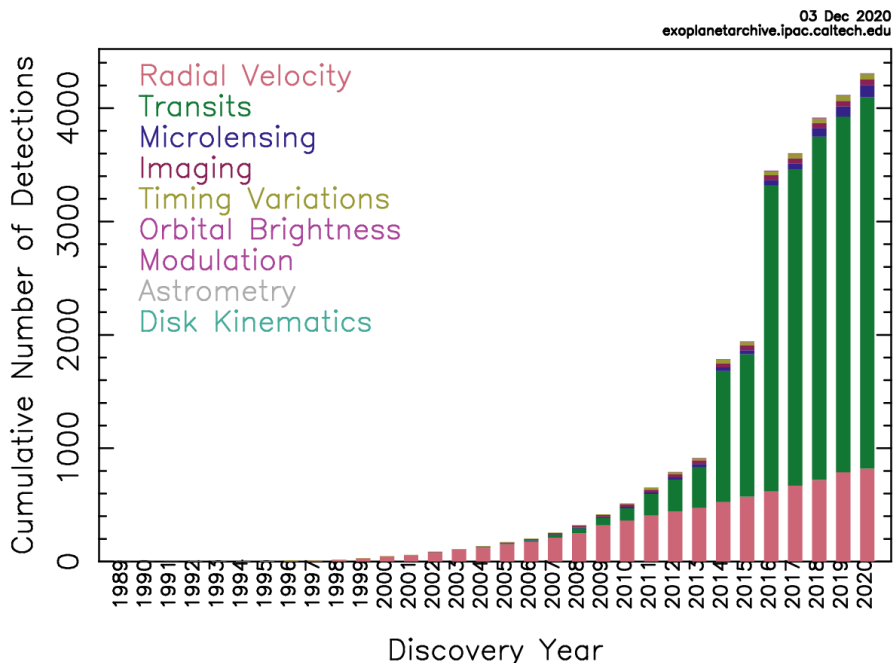


Figure 1: Cumulative exoplanet detections for the major detection methods per year. RV and transits make up the bulk of the discoveries.

increases until the contribution from both the star and the planet reaches a maximum. During the secondary eclipse the planet becomes occulted by the star and the only flux observed is from the star alone. If the star’s size can be determined to a considerable accuracy from its spectrum, then the degree at which the flux dips is directly proportional to the size of the orbiting planet. For a Sun-sized star, a planet the size of Jupiter will cause a 1% change in flux, a Neptune-sized planet would create a change of 0.1%, and an Earth-sized planet will cause a change of 0.01%. Different techniques can be used depending on the orbital phase to reveal various planetary properties.

A transmission spectrum is observed during the primary transit and is used to discern the nature of the planet’s atmosphere. The starlight passing through the planet’s atmosphere is blocked preferentially at wavelengths where the atmosphere is absorbing. At wavelengths with higher atmospheric absorption, the planet appears larger. This observed size is essentially a transmission spectrum of the atmosphere at the planets terminator — or the line separating the day/night sides. The structure and composition of the atmosphere is analysed using this technique.

An emission spectrum is obtained during the secondary transit/eclipse, where the emergent spectrum due to the day-side atmosphere is observed (Knutson et al., 2007a, 2009). Just before the planet passes behind the star the combined spectrum is measured. This spectrum is then subtracted from the stellar spectrum taken during the secondary eclipse to leave the only the planetary spectrum. Ground-based, infrared (IR) observations of secondary eclipses are inherently difficult due to Earth’s atmosphere but it is possible to detect very hot exoplanets. Secondary eclipse depths at these wavelength can be as big as 0.1% relative to the star (which is considered a large signal).

As the planet orbits between its primary and secondary transits, a phase curve is generated – as seen in the bottom of Figure 2 and the real data plotted in Figure 3 (Stevenson et al., 2014). The lightcurve in Figure 3 is plotted as normalized flux over the orbital phase, where a normalized flux of 1 (dotted line) is the flux solely from the host star. The secondary eclipse can be seen at orbital phases 0.5 and 1.5 and the primary is at phase 1. Notice the increased flux due to the illuminated day side of the planet during its orbit. This plot also highlights how the shape of a lightcurve in two different bandpasses (3.6 and 4.5  $\mu\text{m}$ ) and on two different visits in the same bandpass (3.6  $\mu\text{m}$ ) can vary. These phase curve observations can give a wealth of information about the exoplanet’s atmosphere including: cloud formation, energy balance and atmospheric dynamics (e.g., winds).

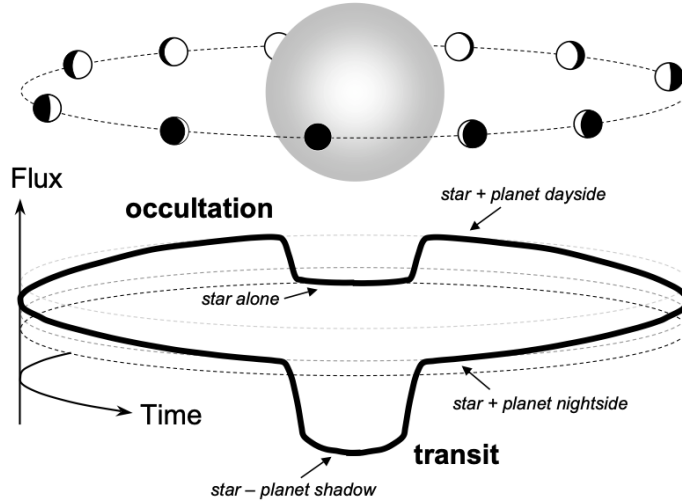


Figure 2: The schematic of an orbiting planet’s path around its host star and the resulting lightcurve. A lightcurve is produced when a planet passes in from if its host star and the flux is plotted as a function of time. Image Credit: (Winn, 2014)

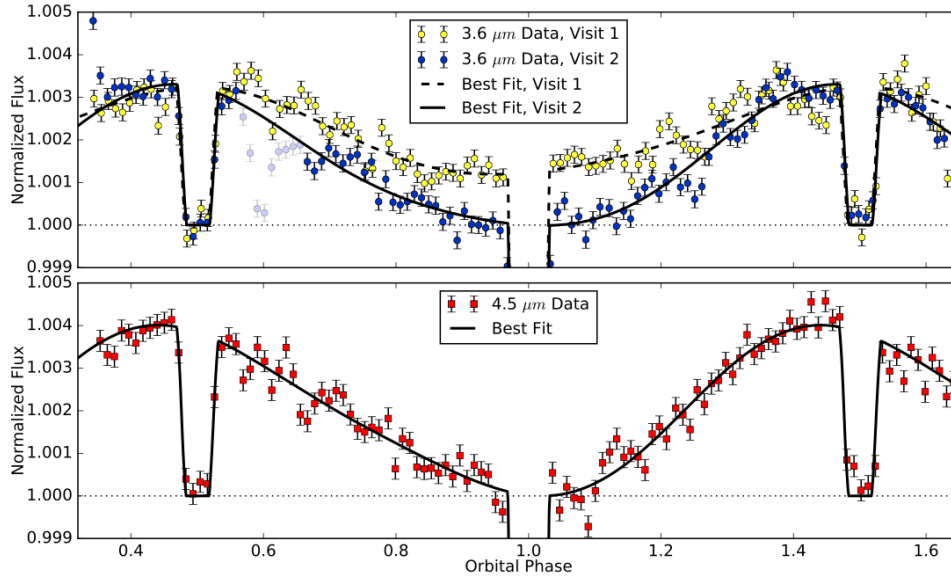


Figure 3: Phase curves measured for the highly irradiated HJ WASP-43b in the 3.6 and 4.5  $\mu\text{m}$  bands of *Spitzer*. The primary transit happens at phase 1.0 and the secondary eclipses are at phase 0.5 and 1.5. Deming et al. 2019 suggests that the two visits in the 3.6  $\mu\text{m}$  band differ due to the possibility of clouds. Image credit: (Stevenson et al., 2017)

Wide-field surveys are responsible for finding the majority of the known transiting systems. This is because they study a large number of stars at once, as there is no way of knowing before-hand which stars will have planets in a favorable transiting orientation. This aligned orbit is one of the geometric challenges in using this method. The probability of observing a transit is inversely related to the distance between the planet and its star and proportionally related to the radius of the star. Using the transit technique, telescopes from both space and the ground have found and continue to find amazingly diverse systems that have completely changed how we think about the uniqueness of our own Solar System.

### 2.1.2 Radial Velocity

The RV method, or sometimes called Doppler spectroscopy, takes advantage of the Doppler shift effect and is responsible for finding the first exoplanets. The Doppler shift phenomenon can be written,

$$f' = f \left( \frac{v \pm v_o}{v \pm v_s} \right), \quad (1)$$

where  $f$  is the frequency of the source,  $f'$  is the Doppler frequency,  $v$  is the speed of the wave,  $v_o$  is the speed of the observer (can be + if the observer is moving toward source or - if the observer is moving away from the source), and  $v_s$  is the speed of the source (can also be + or -). When the source is moving towards a stationary observer the apparent frequency is larger relative to the actual frequency and a shorter wavelength,  $\lambda$ , is observed (recall  $f \propto 1/\lambda$ ). Alternatively, when the source is moving away from a stationary observer the apparent frequency is smaller than the actual frequency and a larger wavelength is observed. As seen in Figure 4, when a star orbits the common center of mass between itself and a planetary companion, it periodically moves toward and away from an observer and its spectral lines become displaced.

Spectrographs from both space and the ground are used to monitor stars and look for periodic shifts in their spectra which can indicate orbiting companions. Their precision has greatly advanced over the last few decades. They have gone from detecting RV shifts on the order of  $\approx 10 \text{ m s}^{-1}$  (on the order of detecting a Jupiter-sized planet) to  $\approx 10 \text{ cm s}^{-1}$  (on the order of detecting a Earth-sized planet). A huge benefit from determining the RV of the star is that the mass can be obtained. This mass measurement, however, is highly dependent on viewing angle. The relationship between mass ( $M$ ) and the inclination ( $i$ ) is:

$$M_{\text{true}} = \frac{M_{\text{min}}}{\sin i} \quad (2)$$

where  $M_{\text{true}}$  is the true mass and  $M_{\text{min}}$  is the minimum mass. When viewing the system edge on ( $i = 90^\circ$ ), the star's velocity amplitude reaches maximum and minimum distance from the observer and thus the true mass can be found since  $M_{\text{true}} = M_{\text{min}}$ .

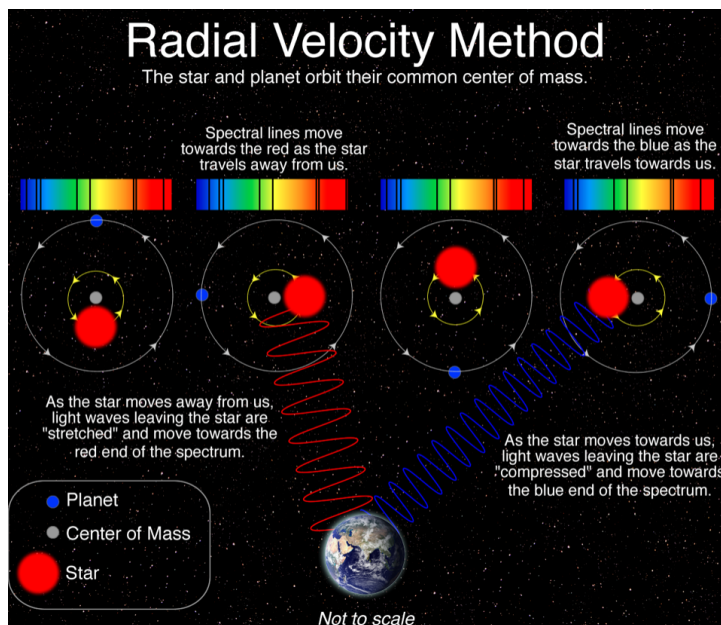


Figure 4: Diagram detailing the Radial Velocity (Doppler Shift) method. Credit: Las Cumbres Observatory

### 2.1.3 Microlensing

As light travels from a distant star, the gravity of a planet passing between that star and Earth will bend and focus it. This is called gravitational microlensing and was first suggested as a exoplanet hunting technique in 1991 (Mao and Paczynski, 1991). Microlensing is especially well-suited for finding low-mass planets that orbit distant or dim stars. A Jupiter-sized exoplanet was the first to be found (Bond et al., 2004) via this technique and more recently, the  $\sim 3 M_E$  (Earth mass) exoplanet OGLE 2016-BLG-1195 was discovered (Bond et al., 2017). In total, there has been 10 exoplanets in 9 systems found using gravitational microlensing.

### 2.1.4 Imaging

The direct imaging technique is capable of spatially resolving the exoplanet from its host star. Because stars will outshine their exoplanetary companions at small semi-major axis, only planets that lie on the outer edges of their systems can be found via imaging. The combination of a large telescope and an adaptive optics system has created high-contrast images of massive exoplanets lying far from their host stars (Macintosh et al., 2015). Both the transit and RV methods are unable to probe the wide separation distances of exoplanetary systems that direct imaging can. Viewing systems at these distances can especially shed light on planet formation and

evolution. Direct imaging surveys have developed better constraints on selecting targets over the last decade and thus maximizing the detection of companions of planetary mass (Nielsen et al., 2013, 2019a).

### 2.1.5 Timing Variations

Transits, eclipses from binary stars, and natural pulses from stars are predictable events in time. The detection of variations in these periodic intervals – or timing variations – can be a result of a companion exoplanet gravitationally affecting the system. In fact, this is the exact method used by Urbain Le Verrier to theoretically predict the presence and location of Neptune from its affect on Uranus’ motion in 1846 (Le Verrier, 1846). In 2011, Sarah Ballard et al. (2011) were the first to discover the exoplanet Kepler 19c using this technique. The variations in the transit timing of its known companion Kepler 19b were found to be offset by five minutes when compared to an unperturbed system. Follow-up RV measurements had to confirm the perturbing planet since the inclination of the orbital plane was not sufficiently large to produce a transit.

When there is an orbital resonance occurring between two planets, transit timing variations are more likely to be detected. A resonance occurs when the ratio of the orbital period of the two bodies are whole numbers. For example, in a 2:1 resonance the inner planet orbits the host star two times for every one orbit that the outer planet makes. When the resonant planets align with each other they are the closest thus resulting transit time offsets are the strongest. Using this method, it is possible to detect Earth-mass exoplanets from current ground and spaces based observatories (Agol et al., 2005). As of January 2021 NASA Exoplanet Archive lists 21 exoplanets found via the transit timing variation method, 16 using the eclipse timing variation method, 7 with the pulsar timing variation method, and 2 with the pulsation timing variation.

## 2.2 Exoplanet Demographics

Properties of the planets (e.g., mass, radius, orbital properties), their host stars (e.g., temperature, mass, radius, luminosity, age, activity) and the system’s environmental properties are just few of the parameters that influence planet formation and evolution. Current views on exoplanet demographics are nicely summarized in a recent review (Gaudi et al., 2020). Ultimately, planet formation and evolution theories can be vetted with the distribution functions produced by these fundamental parameters.

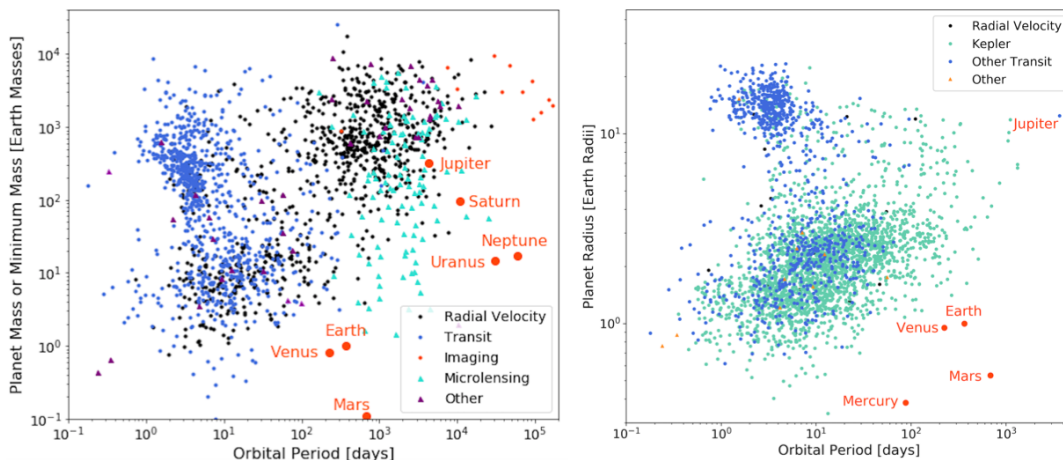


Figure 5: Distributions of approximately 4300 exoplanetary mass objects around stars with their mass (left) and radius (right) as a function of their orbital periods. Different colors indicate the detection method used for discovery. It is important to note that there are both real features and some induced by selection effects. Because RV measurements are needed to make a mass estimate, there is a large population of small (1-4 Earth radii) planets in the right plot that are absent in the left plot. This is because the majority of Kepler field stars are incredibly faint and thus challenging to observe with the radial velocity technique. Figure adapted from (Gaudi et al., 2020) and based on data taken from NASA Exoplanet Archive.

Figure 5 shows some interesting properties of the known planets to date. Selection biases play an important role in exoplanet demographics surveys and thus should be considered carefully. The majority of exoplanets found by way of the transit method are detected at small semi-major axis from their host stars, as seen in the left panel. This bias from the transit method is due to the higher probability of transit at shorter separation distances and thus smaller periods. It is curious why RV surveys have seemingly missed this population of exoplanets since these HJs should increase their sensitivity. Gaudi et. al (2005) took a closer look at this problem and demonstrated that when both small-number statistics and selection biases were taken into account there is agreement between the two survey methods. They report that the distribution in periods found from

each method are consistent to better than the  $1\sigma$  level. Stellar glare obscures detection of exoplanets at small semi-major axis from direct imaging and the exoplanets found using this technique are located at distances  $\geq 4$  AU, highlighting the current instrument performance. A large majority of RV detected exoplanets have masses and radii similar or larger than Jupiter. These massive planets exert a larger stellar reflex motion on their host star, making them easier to detect. On the bottom right of the left figure notice that there are a dearth of objects missing. This is due to the fact that the current detection methods mentioned here have been unable to probe this area of parameter space. The observational biases seen today should lessen as instruments and analysis techniques grow increasingly more advanced and large-scale surveys continue to monitor stars.

In summary, the various detection techniques have all helped to make major discoveries in exoplanet population studies. Recent statistical analyses from RV surveys (Howard et al., 2011; Mayor et al., 2011; Johnson et al., 2010; Bonfils et al., 2013; Fernandes et al., 2019) have found broad agreement in the following properties of the exoplanet population:

- Giant planet occurrence rates around Sun-type stars increases with orbital periods up to approximately 5 years or a separation of about 3 AU. In the protoplanetary disk this correlates to the snow-line. The snow-line is a boundary centered around the star beyond which any water present will freeze into ice. Beyond this the occurrence rate begins to decline.
- The mass function of low-mass exoplanets rises rapidly for short period ( $< 50$  days) exoplanets around Sun-type hosts. In this period range, super-Earths and sub-Neptunes are over an order of magnitude more frequent than giant exoplanets.
- At separations of 2.5 AU and less, the giant planet occurrence rate increases with stellar mass and metallicity.

Statistical analyses of large transit surveys, specifically *Kepler*, have found the following interesting properties:

- There is a bi-modal distribution in size in the small planet regime that separates rocky super-Earths from mostly gas sub-Neptunes. Orbital distance and the mass of the host star are two crucial factors that create this distribution (Fulton & Petigura, 2018).
- There exists an absence of short-period (possibly up to 5-10 days) Neptune sized planets — a so called “Neptune desert” (Mazeh et al., 2016).
- Multi-planet systems are more likely to have planets that are all roughly the same size. There also tends to be regular spacing in systems with three or more planets (Weiss et al., 2018).
- There is an association between short period, HJs and hosts stars with high metallicity (Petigura et al., 2018).

Direct imaging surveys have revealed the following through statistical analyses:

- Gas giants at separations greater than 10-50 AU are uncommon.
- It appears that gas giants that are 1-15  $M_J$  and in large orbits are more commonly found around higher mass stars (Vigan et al., 2020).
- M dwarf host stars are more likely to harbor brown dwarf companions between 20–76  $M_J$  when compared to higher mass stars (Nielsen et al., 2019b).

## 3 Characterizing Exoplanets via Transits

### 3.1 Orbital Elements

A Keplerian orbit, named after 17<sup>th</sup> century astronomer Johannes Kepler, is an idealized orbit and is appropriate for two-body systems, except when General Relativity is important close to a star.

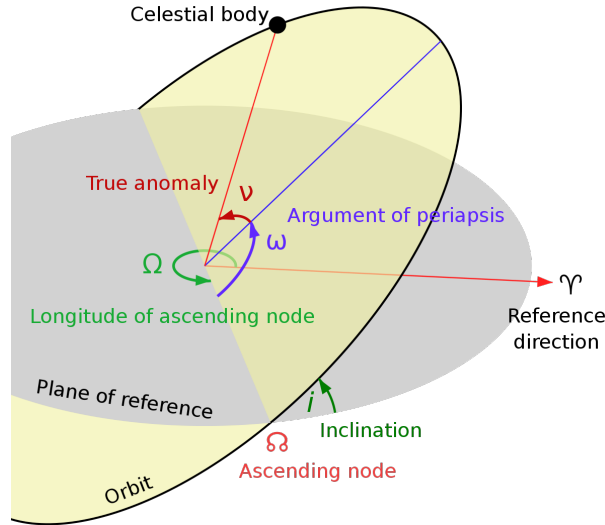


Figure 6: This diagram describes the fundamental orbital elements of a two-body system. The reference plane is shown in gray and the orbital plane is yellow. Where the two planes intersect is called the line of nodes. The ascending node is where the orbit passes upward through the reference plane and the descending node is the downward passage. A reference frame is established with the combination of the vernal point and the reference plane. Image: Lasunncty

In an inertial reference frame, there are seven parameters or orbital elements that define an orbit, as shown in Figure 6.

1. **Semi-major axis** ( $a$ ) - the distance between the centers of the bodies at their furthest distance from each other.
2. **Eccentricity** ( $e$ ) - the measurement of how the shape of the orbit deviates from a circle. The eccentricity of a perfect circle is 0, an eccentricity between 0 and 1 is elliptic, and anything over 1 is hyperbolic.
3. **Inclination** ( $i$ ) - the minimum angle created between the the orbital plane and the reference plane in the vertical direction. Close to  $90^\circ$  for near edge-on observations.
4. **Longitude of the ascending node** ( $\Omega$ ) - angle on the reference plane that is measured from the reference frame's vernal direction ( $\Upsilon$ ) to the ascending node ( $\Upsilon$ ) to orientate the ellipse.
5. **Argument of periapsis** ( $\omega$ ) - the angle on the orbital plane that is measured from the ascending node to the periapsis to orientate the ellipse.
6. **Epoch** ( $t_o$ ) - a specified time.
7. **Period** ( $P$ ) - the time it takes for one object to make a complete orbit around another object.

The true anomaly ( $\nu$ ) is the angle on the orbital plane that defines the orbiting body's position relative to the primary body at a specified time.

## 3.2 Basic Equations

### 3.2.1 Eclipse Geometry

Consider a star with mass  $M_*$  and radius  $R_*$  being orbited by a planet of mass  $M_p$  and radius  $R_p$ . Figure 7 displays the close-up geometry of a transiting body and lightcurve. The coordinate system is centered on the star, with the sky on the X-Y plane and the +Z-axis pointing out towards the observer. The X-axis is aligned with the line of nodes, with the planetary orbit's descending node along the +X-axis (making  $\Omega=180^\circ$ ). This figure highlights the importance of the the impact parameter, depth, and timing of events on the light curve – all of which I will describe in greater detail in this section.

#### Impact Parameter

The *impact parameter* is the sky-projected distance between the center of the planetary disk and the stellar disk at conjunction — or the point, as viewed from an observer, at which the two objects are the most closely aligned. It is defined as:

$$b = \frac{a \cos i}{R_*} \left( \frac{1 - e^2}{1 + e \sin \omega} \right). \quad (3)$$

Its value ranges as  $0 \leq b \leq 1$ . The maximum transit duration happens when  $b = 0$  and is when the planet transits the center of the stellar disk. So, as  $b$  increases the total transit time decreases. Grazing transits occur at high  $b$  values where the planetary disk falls out of the stellar disk for the entire transit.

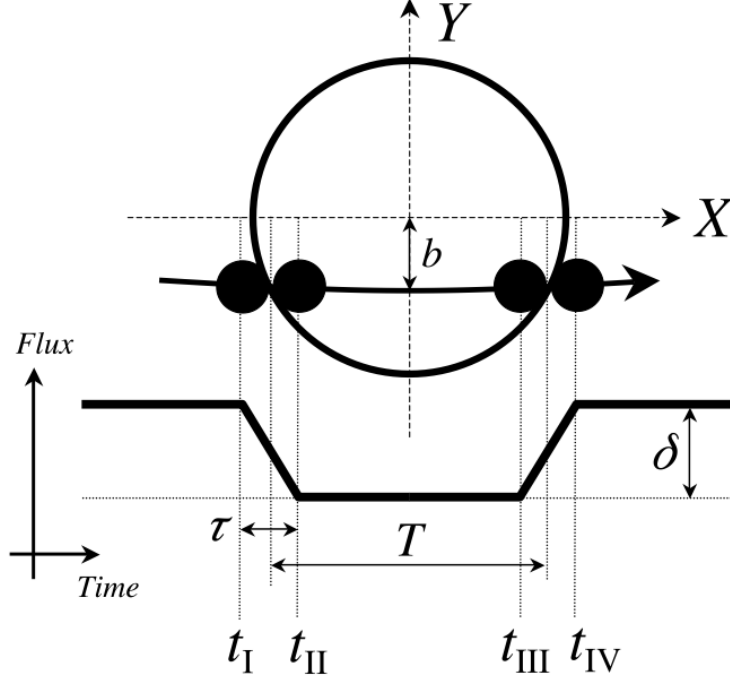


Figure 7: Illustration of a transit and corresponding lightcurve that identifies the contact points ( $t_I - t_{IV}$ ), the transit depth ( $\delta$ ), the halfway points of ingress and egress ( $T$ ), and the time of ingress and egress ( $\tau$ ). Image Credit: (Winn, 2014).

### Contact Times

The transit event contact times  $t_I - t_{IV}$  are shown in Figure 7. The first contact ( $t_I$ ) occurs the moment the planetary disk begins entering the stellar disk and the second contact ( $t_{II}$ ) occurs when the planetary disk is fully inside the stellar disk. The *ingress* ( $\tau$  between  $t_I$  and  $t_{II}$ ) is defined as the transition time from first to second contacts. Similarly, the third contact ( $t_{III}$ ) is the last moment that the planetary disk is fully inside the stellar disk and the fourth contact ( $t_{IV}$ ) occurs when the planetary disk has fully left the stellar disk. Similarly, the *egress* ( $\tau$  between  $t_{III}$  and  $t_{IV}$ ) is defined as the transition time from third to fourth contacts. The total transit duration can be found as:

$$T_{\text{tot}} \equiv t_{IV} - t_I = \frac{P}{\pi} \sin^{-1} \left[ \frac{R_*}{a} \frac{\sqrt{\left(1 + \frac{R_p}{R_*}\right)^2 - b^2}}{\sin i} \right]. \quad (4)$$

The full transit duration can be found as:

$$T_{\text{full}} \equiv t_{III} - t_{II} = \frac{P}{\pi} \sin^{-1} \left[ \frac{R_*}{a} \frac{\sqrt{\left(1 - \frac{R_p}{R_*}\right)^2 - b^2}}{\sin i} \right], \quad (5)$$

Another important timescale describing the interval between ingress and egress times shown in Figure 7 is  $T \equiv T_{\text{tot}} - \tau$ . Results are further simplified in the limits of  $e \rightarrow 0$ ,  $R_p \ll R_* \ll a$  and  $b \ll 1 - (R_p/R_*)$  (full transits only) as:

$$T \approx T_o \sqrt{1 - b^2}, \tau \approx \frac{T_o \left(\frac{R_p}{R_*}\right)}{\sqrt{1 - b^2}}, \quad (6)$$

where  $T_o$  is defined as the characteristic timescale

$$T_o \equiv \frac{R_p P}{\pi a} \approx 13 \text{ hr} \left( \frac{P}{1 \text{ yr}} \right)^{1/3} \left( \frac{\rho_*}{\rho_\odot} \right)^{-1/3}. \quad (7)$$

Here we see that the stellar density,  $\rho_*$ , can be found via the transit lightcurve! More on this in a bit.

### 3.2.2 Geometric Transit Probability

To observe an eclipse event, the observer must be lucky enough to view the system near edge-on. Figure 8 depicts a planet orbiting its star and the shadow band at which the transit can be seen by a distant observer. The opening angle of this cone ( $\Theta$ ) satisfies the condition of  $\sin \Theta = (R_* + R_p)/r$  and  $r$  is the instantaneous star-planet distance. The thick black lines of the cone map out the shadow band – or penumbra. In this area both grazing and non-grazing transits are visible. Inside the penumbra cone, the thin black lines map out another cone called the antumbra which is described by  $\sin \Theta = (R_* - R_p)/r$ . In this area just the full transit is visible.

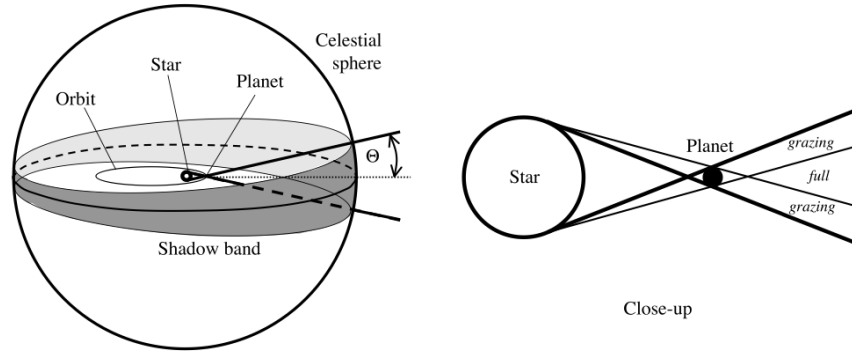


Figure 8: Visual illustrating how the transit probability is calculated. *Left:* The opening angle of the cone,  $\Theta$  (where  $\sin \Theta = (R_* + R_p)/r$  and  $r$  is the instantaneous star-planet distance), sweeps out a band on the celestial sphere. A transit will be observed if an viewed from within this shadow band (penumbra) of the planet. *Right:* A close-up of the system with the penumbra (full + grazing transit visible) indicated in thick black lines and antumbra (only full transit visible) in thin lines. Image Credit: (Winn, 2014)

The transit probability is found using Equation 3 and the understanding that, for an observer placed at random,  $\cos i$  is uniformly distributed.

$$p = \left( \frac{R_* \pm R_p}{a} \right) \left( \frac{1 + e \sin \omega}{1 - e^2} \right), \quad (8)$$

where the signs indicate the allowing of grazing eclipses (+) and the exclusion of them (-). In the case where  $e = 0$  and  $R_* \gg R_p$  this reduces nicely to

$$p = \frac{R_*}{a} \approx 0.005 \left( \frac{R_*}{R_\odot} \right) \left( \frac{a}{1 \text{ AU}} \right)^{-1}. \quad (9)$$

### 3.2.3 Flux Variations During Eclipses

The flux throughout a transiting exoplanet's orbit can be succinctly written as:

$$F(t) = F_p(t) + F_*(t) - \begin{cases} 0 & \text{if outside eclipse,} \\ F_*(t) \beta_{\text{tra}} \left( \frac{R_p}{R_*} \right)^2 & \text{during transit,} \\ F_p(t) \beta_{\text{occ}} & \text{during occultation.} \end{cases} \quad (10)$$

Here,  $F_p$  and  $F_*$  are the fluxes of the planet and the star, respectively.  $F_*$  can change over time as the star experiences activity (i.e, flares, star spots, plages). The dimensionless functions  $\beta$  in both the transit and the occultation equations are of order unity depending on the overlapping area between the planetary and stellar disks.

### 3.2.4 Characterizing the System

Analytical equations given in Seager & Mallen-Ornelas (2003) describe the geometry of the transit in terms of the observables ( $\delta$ ,  $T_{\text{tot}}$  and  $T_{\text{full}}$  (or  $T$  and  $\tau$ )) and the important quantities derived from them ( $b$  and scaled stellar radius over the semi-major axis ( $R_*/a$ )). The transit times (Equations 5 and 4) can be inverted then simplified in the limits where  $R_p \ll R_* \ll a$  and  $b \ll 1 - (R_p/R_*)$  (full transits only). The formulae are:

$$\Delta F = \frac{F_{\text{no transit}} - F_{\text{transit}}}{F_{\text{no transit}}} = \left(\frac{R_p}{R_*}\right)^2 = \delta, \quad (11)$$

$$b^2 = 1 - \sqrt{\delta} \frac{T}{\tau}, \quad (12)$$

$$\frac{R_*}{a} = \frac{\pi}{\delta^{1/4}} \frac{\sqrt{T\tau}}{P} \left(\frac{1 + e \sin \omega}{\sqrt{1 - e^2}}\right). \quad (13)$$

Additional complications such as limb darkening have important implications for the transit lightcurve and must be treated carefully, but to first order this simple expression holds. From these, the planet  $i$  projected on the sky plane and the combination of stellar and planetary mean density ( $\rho_*$  and  $\rho_p$ , respectfully) can be found:

$$i = \cos^{-1} \left(\frac{bR_*}{a}\right). \quad (14)$$

$$\rho_* + \rho_p \left(\frac{R_p}{R_*}\right)^3 = \frac{3\pi}{GP^2} \left(\frac{a}{R_*}\right). \quad (15)$$

The left side of Equation 15 simplifies further, as the cubed ratio of  $R_p/R_*$  is commonly small, and thus  $\rho_*$  can be determined directly from the transit data.

Planetary radius from the transit lightcurve can be combined with a mass measurement to gain insights on planetary composition. Since the photometry during the transit us tells nothing regarding mass, one needs RV measurements or, more specifically, the velocity semi-amplitude ( $K_*$ ). This can be found using the equation described in (Winn, 2014):

$$\frac{M_p}{(M_p + M_*)^{2/3}} = \frac{K_* \sqrt{1 - e^2}}{\sin i} \left(\frac{P}{2\pi G}\right)^{1/3} \quad (16)$$

Note that the RV method (Section 2.1.2) relies on  $i$ , as exoplanets viewed perfectly edge on ( $i = 90^\circ$ ) will give the most accurate mass measurement. Transiting planets have an inclination close to  $90^\circ$ , allowing  $\sin i \approx 1$ .

### 3.2.5 Characterizing the Atmosphere

#### Scale Height

With reference to Seager (2010), a planet with an atmosphere in hydrostatic equilibrium has a pressure:

$$P = nkT = P_0 e^{-z/H}, \quad (17)$$

where  $z$  is the altitude and  $H$  is the *atmospheric scale height*. This is the measurement of the height of the atmosphere about the surface. Due to the nature of an atmosphere having a non-defined edge, this distance is the height at which the pressure in the atmosphere decreases (with respect to the surface pressure) by the value  $e \approx 2.71828$ . It can be written as:

$$H \equiv \frac{kT}{\mu g_p}, \quad (18)$$

where  $k$  is the Boltzmann constant,  $T$  is the temperature,  $\mu$  is the mean molecular weight, and  $g_p$  is the acceleration due to gravity from the planet ( $G_p \equiv GM_p/R_p^2$ ).

#### Spectral Slopes

In a transmission spectra, a *spectral slope* is a rise in  $\delta$  towards the blue in the optical wavelength (the planet appears to have a larger radius in blue vs red wavelengths). This slope is evaluated by (e.g., Lecavelier Des Etangs et al. 2008) as:

$$\frac{dR_p}{d \ln \lambda} = H\alpha, \quad (19)$$

where  $R_p$  is the planetary radius,  $\lambda$  is the observing wavelength,  $H$  is the scale height, and  $\alpha$  is the spectral index of atmospheric opacity, i.e.,  $\kappa \propto \lambda^\alpha$ . Observed spectral slopes are often associated to Rayleigh scattering ( $\alpha = -4$ ) caused by small aerosols with more negative  $\alpha$  values corresponding to steeper slopes.

### 3.2.6 Limb Darkening

The transit lightcurve is influenced by both the planetary parameters and the stellar surface structure. Therefore, an accurate model accounts for both. One of the most important parameters on a stellar surface model is limb darkening (e.g., (Pont et al., 2007; Wolter et al., 2009)). The inconsistent surface brightness across the stellar disk results in it being brightest at its center and dimmer at its edges, or limbs. The photons coming from the center of the disk originate from deeper in the stellar atmosphere than the photons from the edge, making them hotter and appearing brighter. This is the mechanism behind limb darkening. The shape of the limb darkening is extremely important when modeling transit lightcurves as it will influence the derived planetary parameters — especially  $R_p$  and  $b$ . Specifically, it blurs  $t_{II}$  and  $t_{III}$  (Winn, 2014). The literature provides different limb darkening laws (or fitting functions) that describe the variation of intensity observed in the stellar disk: the linear law, quadratic law, square root law, logarithmic law, non-linear law (Claret, 2000), and the 3-parameter non-linear law (Sing, 2010). With regard to transit lightcurves, the quadratic law is the most common as it works well for a large range of stellar effective temperatures (Mandel and Agol, 2002). The quadratic law is formally written as

$$\frac{I(\mu)}{I(\mu=1)} = 1 - u_a(1 - \mu) - u_b(1 - \mu)^2, \quad (20)$$

where  $I(\mu=1)$  is the intensity in the middle of the stellar disk,  $\mu = \cos(\theta)$  ( $\theta$  = angle between line of sight and the emergent star light),  $u_a$  and  $u_b$  are the quadratic limb darkening coefficients. Figure 9 shows the geometric interplay between the limb darkening equation parameters.

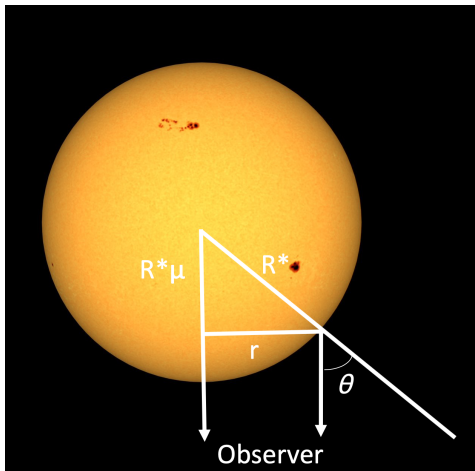


Figure 9: Geometry of the parameters involved in limb darkening on an image of the Sun. As  $\theta$  increases,  $\mu$  decreases, or  $r$  increases, the flux from the star falls off. Image Credit: NASA

It is helpful to graphically visualize the affects of limb darkening on a transit profiles of different stellar types in the *ugriz* broad-band filters (spanning  $\sim 0.324$ - $0.711 \mu\text{m}$ ). Model transit lightcurves were generated by *batman* (Kreidberg, 2015) for a planet with the following parameters:  $0.1 R_*$  (Jupiter-sized),  $P=3$  days,  $a = 15 R_*$ ,  $e = 0$ ,  $\omega = 90^\circ$ , and a star with  $\log(g) = 4$ ,  $[\text{Fe}/\text{H}] = 0$ ). Figure 10a plots the three main fitting functions used to model limb darkening and compares them to a uniform stellar disk. The uniform disk lightcurve has a noticeably boxy, nonphysical shape with a steeper ingress/egress relative to the rounded-bottom lightcurves treated with a limb darkening fitting function. Figures 10b - 10f show multi-broadband lightcurves across host stars of stellar types A-M ( $T_{\text{eff}}$  ranging from 8000-2750 K). The quadratic law was chosen for modeling the limb darkening as it is the most commonly used in the field. For A, F, and M stars, the filter lightcurves have similar shapes with the curves getting steeper and more boxy with an increase in wavelength (towards the near-IR  $z$  band). The curves for the G and K stars stand out in that their near-UV and green bands have much shallower transit depths than the longer wavelength bands. The behavior observed in these plots can be explained using a wavelength dependent limb darkening law. This effect of stronger limb darkening at shorter wavelengths has been observed on the Sun (Pierce and Slaughter, 1977) and produced by atmospheric models (Claret, 2004).

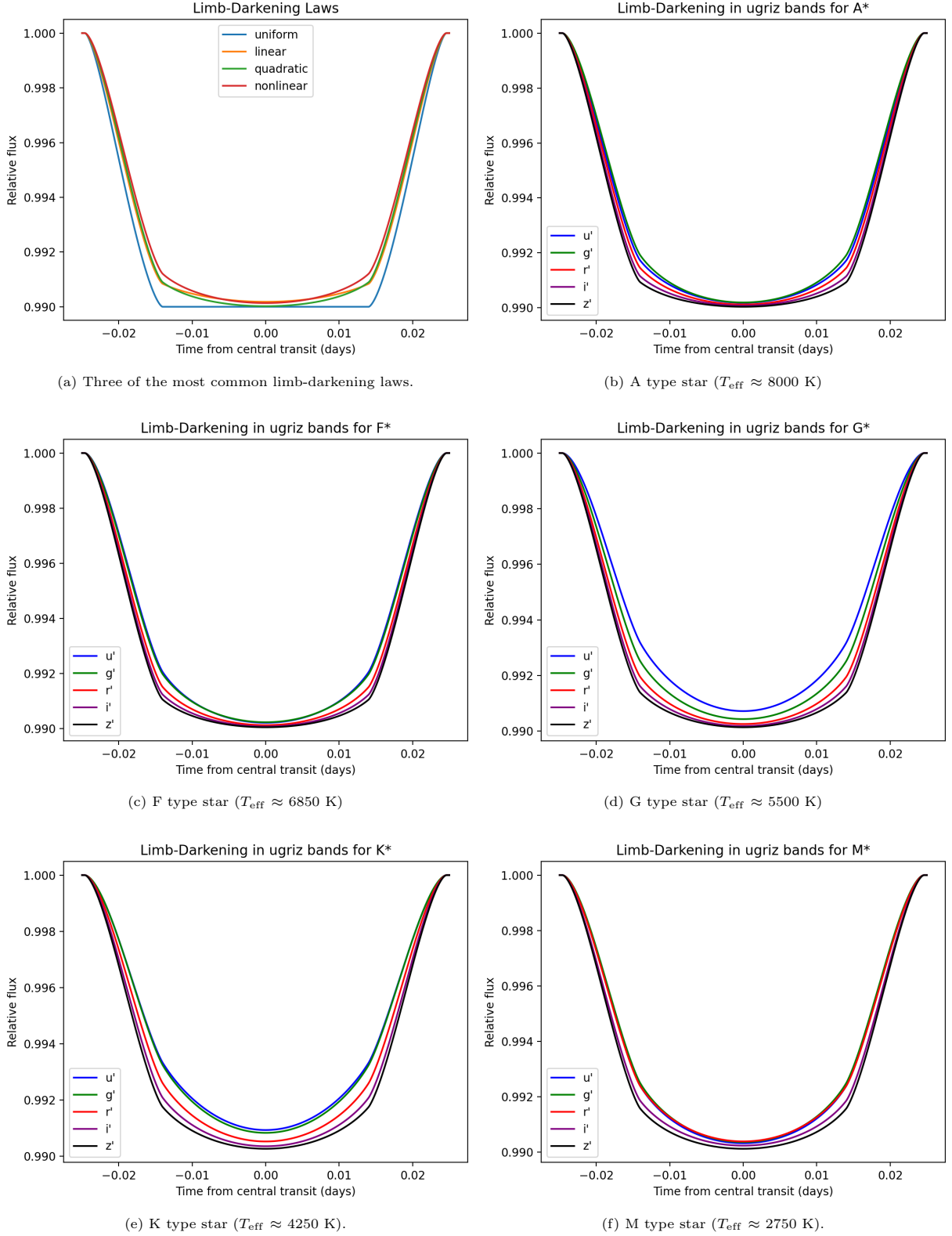


Figure 10: Modeled planetary lightcurves showing limb-darkening effects across varying stellar effective temperatures. Sub-figure (a) shows comparison transit lightcurves of the three most common limb-darkening fitting functions with a uniform stellar disk. Sub-figures (b)-(f) show modeled transit lightcurves using the quadratic fitting function for various stellar types ( $T_{\text{eff}}$  8000–2750 K) in each of the *ugriz* broadband filters.

### 3.3 Stellar Activity

In addition to limb darkening, stellar activity can make the modeling even more complex. This is due to the sensitivity of transit profiles to the distribution of brightness on the stellar surface. This distribution can be both variable in time and spatially inhomogeneous (Knutson et al., 2007b). In contrast to the stellar photosphere, dark spots or bright faculae can either decrease or increase the local brightness. If a spot or faculae is not eclipsed by the transiting planet then there is no direct affect on the transit lightcurve. In this case, just the overall level of the lightcurve is changed. If the transiting planet eclipses the faculae (or spots), then the transit depth would increase (decrease) (Czesla et al., 2009). In both circumstances the effect is wavelength dependent and must be corrected for.

Results have indicated that anomalies in the transit lightcurve can result in an over/under estimation of  $R_p/R_*$  as a function of wavelength by up to 10% and can imitate the scattering of light in the planet’s atmosphere (Oshagh et al., 2014). Figure 11a shows a star spot on the transit lightcurve as a bump near the end of the transition from first to second second contact of HD 189733 b with the stellar disk. As the star rotates, it is both blueshifted and redshifted. This is an effect of the Rossiter-McLaughlin effect (Rossiter, 1924), (McLaughlin, 1924). When the star spot/faculae is located on the side coming towards the observer, as in Figure 11a it can look like atmospheric scattering. Figure 11b shows the corresponding  $R_p/R_*$  as a function of wavelength of HD 189733b. Not fully understanding the stellar activity would make difficult to interpret whether this blue-ward scattering seen on the plot is due to occultation of stellar faculae or Rayleigh scattering through the exoplanet’s atmosphere. The only way to know is to obtain multiple observations of the exoplanet transit event and look for possible variations in the transit depth due to stellar variability.

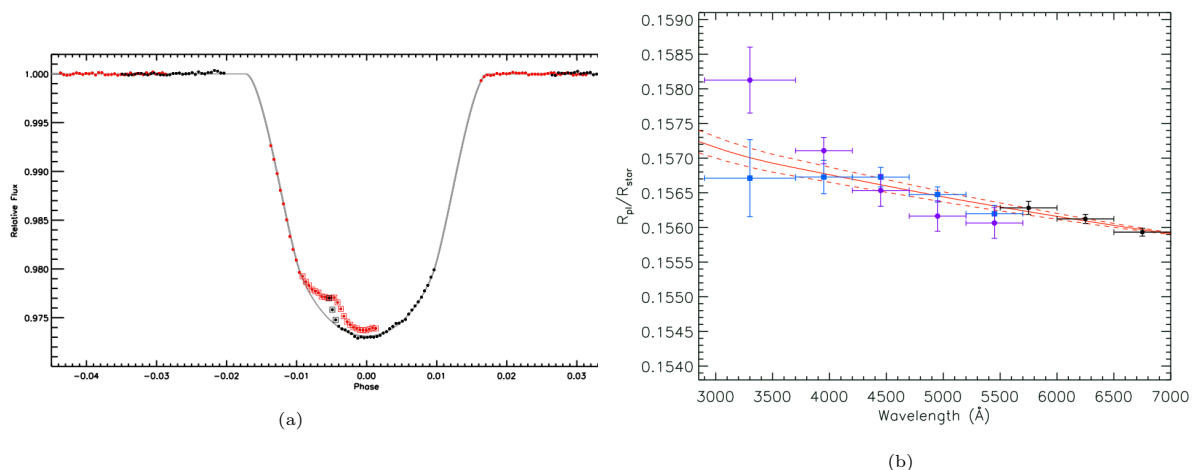


Figure 11: *Left*: White lightcurve from 2 Hubble visits (visit 1 in black and visit 2 in red) of the transit of HJ HD 189733 b. The instrument trends have been removed and the boxes indicate points the eclipsed spot features. Using the un-spotted data points, the best fit to the transit was found and is shown here in grey. *Right*: The radius ratio  $R_p/R_*$  as a function of wavelength for HD 189733 b. There is scatter towards the blue side of the spectrum due to the star spot seen on the lightcurve on the left which can be mistakenly interpreted as Raleigh scattering through the exoplanet’s atmosphere. Image Credit: (Sing et al., 2011b)

### 3.4 Exoplanet Modeling

Current exoplanet modeling techniques are extensive in planetary and stellar properties. The Exoplanet Modeling and Analysis Center<sup>20</sup> houses a catalog, repository and integration platform for exoplanet characteristics and stellar environments. A variety of codes cover everything from climate model outputs for exoplanetary atmospheres to hydro-dynamical simulation codes.

### 3.5 Hot Jupiters

HJs are defined here as hydrogen-dominated planets having periods of  $P \leq 10$  days, separations from  $\sim 0.03$ – $0.1$  AU, and masses  $\geq 0.25 M_J$ . They are strongly irradiated by their host star, receiving thousands of times more stellar radiation than Jupiter and allowing them to reach temperatures of 1000 K or higher (Showman and Guillot, 2002). When the day-side temperature of the planet exceeds temperatures of  $\sim 2200$  K molecular dissociations in the atmosphere take over (resembling stellar atmospheres) and they become ultra-HJs (Bell and Cowan, 2018; Parmentier et al., 2018). In comparison, warm-Jupiters (WJ) are similar, but have longer orbital periods that extend out to the postulated water ice line at about 1 AU. HJs are fairly common. Approximately

<sup>20</sup><https://emac.gsfc.nasa.gov>

1% of solar neighborhood FGK stars have a orbiting HJ (Marcy et al. 2005; Howard et al. 2012), making them fairly common. Various aspects regarding HJs origin theories and atmospheric properties are briefly covered here but for an in-depth reviews see (Madhusudhan, 2019) and (Fortney et al., 2021).

### 3.5.1 Origin Theories

Before the discovery of the first HJ, Peg 51 b, our Solar System was the basis for understanding planet formation and evolution. This HJ discovery revolutionized our way of thinking and spurred the field to find and characterize exoplanets. Still, over two decades later, there is no consensus on their dominant evolutionary path. Three possible mechanisms have been proposed: in-situ formation, disk migration, and high eccentricity tidal migration. While no individual mechanism can fully explain the population, high-eccentricity tidal migration seems to be the dominant formation pathway (see Dawson and Johnson, 2018).

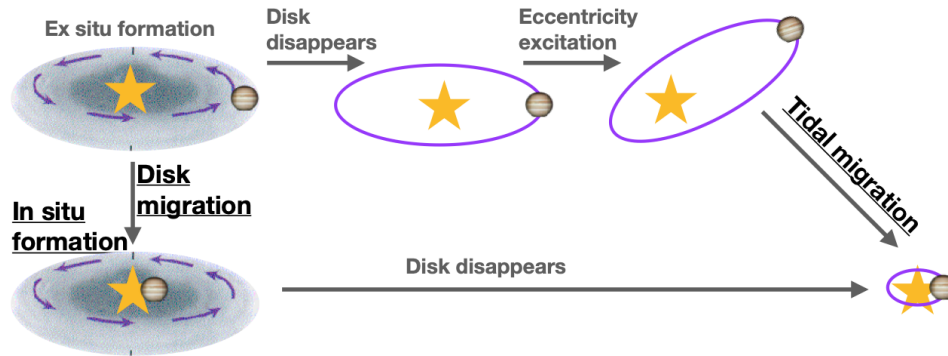


Figure 12: HJ formation theories: in-situ formation, disk migration, and high eccentricity tidal migration. Image credit: (Fortney et al., 2021)

#### In Situ Formation

Whether or not HJs can form at their current small orbital period remains an open question in the field. The gravitational instability and/or core accretion mechanisms for giant planet formation would have to be able to operate at distances very close to the star. Gravitational instability occurs then a fraction of the protoplanetary disk breaks into smaller bound clumps (Durisen et al., 2007). This process requires extraordinarily high gas surface densities and temperatures. Giant planet formation by way of gravitational instability at 1 AU cannot occur since in order to cool precisely, they must be too hot to be bound to the host star (Rafikov, 2005). Thus, this is not a viable option. In the core accretion scenario, a rocky protoplanet core accumulates gas several times its mass from the disk. The challenge for HJs would be to grow a core that is significantly massive enough before the gas in the disk depletes. Giant planets forming close to their star have a thin zone within a disk to accrete matter from, which leads to small core sizes. In order for a large enough core to form a giant planet there must be a better understanding of how solid material gets transported within the disk. Although this formation mechanism is highly criticized, there have been recent studies that have shown several scenarios for in-situ formation of gas giants (e.g., Batygin et al., 2016; Boley et al., 2016). An alternative to in-situ formation is the idea that these planets migrated in to their present day locations.

#### Gas Disk Migration

Torques within the protoplanetary disk are responsible for bringing an initially distant massive planet to hundredths of an AU from its host star (see Baruteau et al. 2014 for an in depth review). Co-rotation torques enable angular momentum to be exchanged between the planet and the disk by way of agitating nearby gas into horseshoe orbits. Lindblad torques then deflect gas further out. The massive planet begins to move inward though, if it migrates faster than the lifetime of the disk, it risks tidal disruption or engulfment by the host star. Just how much of a role gas disk migration plays in HJ formation remains inconclusive due to its high sensitivity to the conditions within the disk.

#### High-Eccentricity Tidal Migration

In gas disk migration the planet's orbital angular momentum and orbital energy are changed simultaneously. In high eccentricity tidal migration, however, they change in a two step process: first decrease the angular momentum then reduce the energy. Many mechanisms have been proposed to describe the reduction of angular momentum. One is planet-planet scattering, where high-eccentricity migration is set off by Keplerian shear being converted into a deficit in angular momentum (Rasio and Ford, 1996). In this scenario the massive planet

would typically have to eject planet after planet in the system thus sending itself into smaller, more eccentric orbits. This type of eccentricity growth by scattering is limited and it has been argued that it must predate the migration of planets into short period orbits (Petrovich et al., 2014). Secular interactions involve the exchange of angular momentum between planets that are widely separated and take place on timescales of thousands or millions of years Petrovich (2015). One type of periodic angular momentum exchange is Kozai-Lidov cycles (Kozai, 1962). These cycles trade off both eccentricity and inclination and have been widely theorized to set off high eccentricity tidal migration of HJs. Once the planet’s eccentricity is adequately large, the orbital energy can be reduced by tidal dissipation in the planet. Tidal dissipation shrinks and then circularizes its orbit while keeping the angular momentum constant.

### 3.5.2 Internal Structure

#### Irradiation and Radius Anomaly

Being so close to their host star, HJs are exposed to intense stellar irradiation. The flux received by the HJs can be upwards of 10,000 times the flux that Jupiter receives from the Sun. Because of this, it may not be surprising that a HJ could have an internal structure that differs from Jupiter. Guillot et al., (1996) first suggested that HJs would not have a means to cool as efficiently over time and thus would have higher internal temperatures and larger radii. This is especially true for HJs that are very close to their host star (0.05 AU) and are tidally locked as a result of very large tidal stresses induced by the host star. Current research has proven this to be the case, but the problem resides in the magnitude of the increased radii (Baraffe et al., 2010). This problem has been dubbed the *radius anomaly* and is a fundamental problem in planetary science (Komacek et al., 2020). Figure 13, adapted from Fortney et al. (2021), displays an evolutionary model of a  $1 M_J$  planet at an age of 4.5 Gyr (red dashed line) with observed planetary radius as a function of incident flux/zero bond albedo equilibrium temperature. Up to temperatures of about  $T_{eq} \sim 1000$  K, observed planets are found mostly scattered below the evolutionary model. These planets are believed to not be experiencing inflated radii due to enhanced metal enrichment (Miller and Fortney, 2011; Demory and Seager, 2011). After  $T_{eq} \sim 1000$  K the incident flux/equilibrium temperature begins increasing with planetary radius – implying a correlation between the parameters. By the time equilibrium temperatures reach  $\sim 1700$  K the majority of observed planets are lying above the evolutionary model and are exhibiting the radius anomaly.

The mechanisms behind HJ inflated radii are reduced into two broad categories: retention of heat in the interior of the planet via reducing the rate of cooling (double diffusive layered convection, slower radiative heat transport in atmosphere) and heating the planet from within via an energy deposit (incident stellar flux converted to deposited heat, tidal dissipation, ohmic dissipation). Sarkis et al. (2020) suggests that there is likely more than one mechanism at play to be able to describe the whole population. It has been found that for non-inflated gas giants with moderate orbital periods ( $p \leq 10$  days), they can re-inflate as their host star begins to evolve off the main-sequence and heat up (Lopez and Fortney, 2016; Grunblatt et al., 2016, 2017). Further studies of HJs orbiting main-sequence and post-main-sequence stars will prove fruitful in constraining the mechanisms behind the radius anomaly (Komacek et al., 2020).

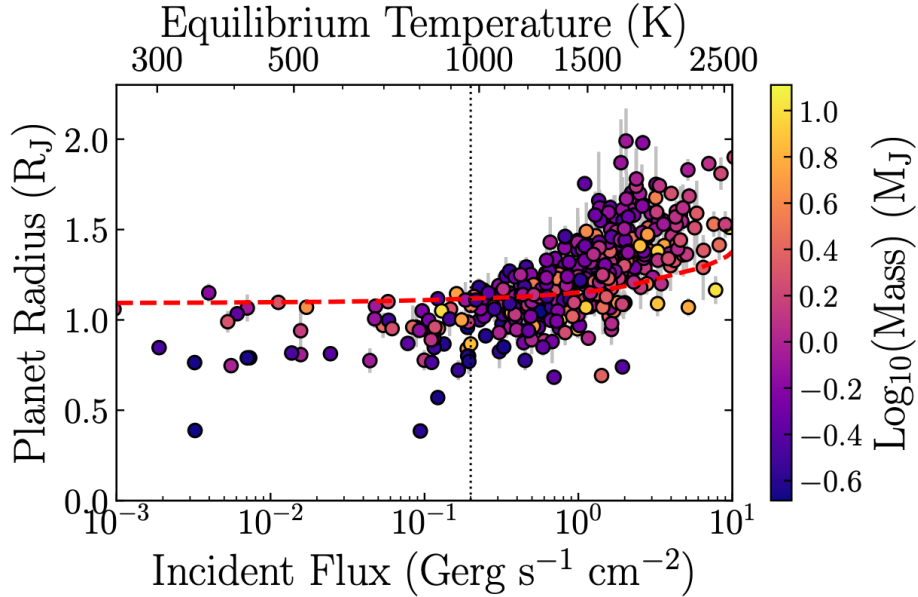


Figure 13: Observed planetary radius as a function of incident flux from the host star for planets with masses from  $0.1 M_J$  to  $13 M_J$ . The dashed red line indicates the evolutionary model for a planet of Jupiter mass with no radial inflation effects at 4.5 Gyr old. The black dotted line indicates the point at which no inflation is found. Figure from (Fortney et al., 2021)

### 3.5.3 Atmospheric Properties

In the last several decades exoplanetary science has rapidly progressed towards more detailed spectroscopic observations to characterize the atmospheres around HJ planets. With the thousands of exoplanets confirmed to date, there exist only  $\sim 50$  that have been targets of detailed atmospheric studies. Recent studies have revealed that exoplanet atmospheres span a continuum – from clear to cloudy. Many are found to have transmission spectra that display a Rayleigh slope of increased absorption at blue wavelengths due to aerosols (i.e., HD-189733b (Gibson et al., 2012) (Pont et al., 2008); WASP-6b (Jordán et al., 2013) (Nikolov et al., 2015)); WASP-12b (Sing et al., 2013); WASP 31b (Sing et al., 2015). Some have been found to exhibit a flat and featureless spectrum, indicative of opaque high altitude clouds (Gibson et al., 2013)(a,b); (Mallonn et al., 2015)(a,b). Still, others have been found to be best explained by a clear atmosphere, where strong spectral features are more pronounced due to composition and temperature conditions (i.e., HD-209458b (Sing et al., 2008); XO-2 b (Sing et al., 2011a)). In each case, observations, theoretical modeling, and retrieval techniques must merge together to provide invaluable understanding into the variety of chemical compositions and physical processes in their atmospheres. Knowing the planetary atmospheric properties is important for constraining geological processes, formation, and migration mechanisms.

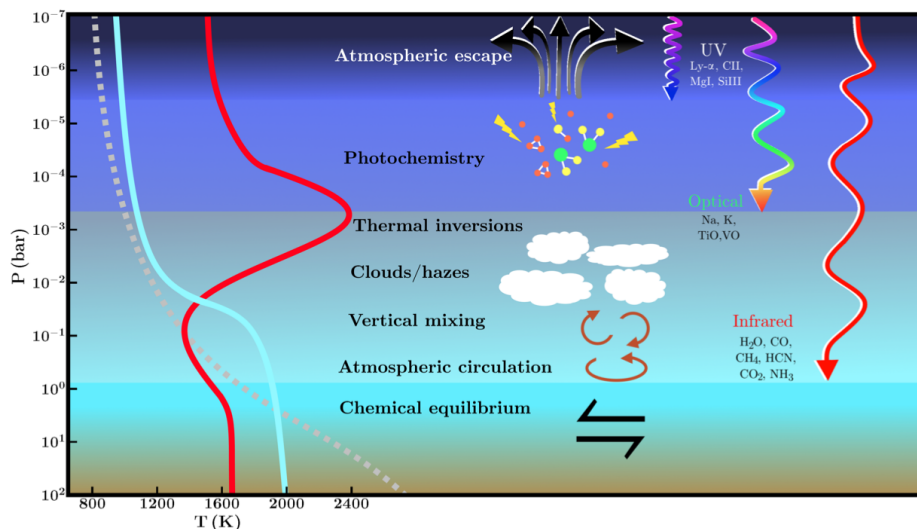


Figure 14: Various components of the electromagnetic spectrum can be used to probe an exoplanet’s atmosphere. The regions of the atmosphere are mapped in units of pressure and the types of penetrating radiation (UV, optical and IR) are shown with arrows on the right. Each atmospheric region has unique physical processes and chemical species that can be investigated. The left side of this plot shows pressure-temperature diagrams for three planets experiencing different atmospheric processes: a poorly irradiated planet (grey, dashed line), a highly irradiated planet with a temperature inversion (red line), and a highly irradiated planet without a temperature inversion (cyan line). Image Credit: (Madhusudhan, 2019)

### Chemical Compositions

Robust chemical detections in the atmospheres of HJs have been found via the primary eclipse and secondary eclipse with high-resolution transmission spectroscopy and direct imaging from both space and ground facilities. Figure 14 illustrates what type of electromagnetic radiation can be used to probe the various layers of an exoplanet’s atmosphere. Electronic transitions by atomic and ionic species show strong absorption in the ultra-violet (UV) and optical. Ionic species probe the exosphere and atomic species help examine the upper regions of the atmosphere, where photochemistry is predominant. Heavier elements such as TiO and VO exhibit strong absorption in the optical. Rotational transitions by volatile molecules show strong absorption in the IR and probe the IR photosphere. Here, thermal inversions, clouds/hazes, vertical mixing and atmospheric circulation dominate. Three atmospheric pressure-temperature profiles are overlaid on the left side of the figure and result from specific atmospheric processes: a highly irradiated planet with a temperature inversion (red), a highly irradiated planet without an inversion (cyan), and a planet being poorly irradiated (grey).

High resolution spectroscopy of transiting HJs have detected many atomic species, e.g., K and Na in the HJ HD 189733b (Wytttenbach et al., 2015) and Ti and Fe in the ultra-HJ Kelt 9b (Hoeijmakers et al., 2018). UV transmission spectra from *Hubble* has detected exospheric hydrogen and heavier elements such as C, O and Mg (Vidal-Madjar et al., 2004; Fossati et al., 2010). Volatile molecules (e.g. CO, CH<sub>4</sub>, H<sub>2</sub>O, HCN, CO<sub>2</sub>) have long been predicted to exist in HJ atmospheres, though this is highly dependent on the C/O ratios, metallicity and temperature (e.g., (e.g., Brogi et al., 2017; Madhusudhan, 2012; Moses et al., 2011)). When it comes to the high temperature atmospheres of HJs, H<sub>2</sub>O and CO have some of the strongest features (Madhusudhan, 2012; Moses et al., 2013). *Hubble* has been instrumental in this area, detecting H<sub>2</sub>O in 10 of 40 HJs to date (Deming et al., 2013; ?; Kreidberg et al., 2014; Sing et al., 2016; Tsiaras et al., 2018) and indications of both HCN and NH<sub>3</sub> (MacDonald and Madhusudhan, 2017).

The molecules present in HJ atmosphere can provide clues to its origin channel (Madhusudhan et al., 2014). The protoplanetary disk has radially spaced volatile condensation fronts (snow-lines) where its composition of gas and dust differs (Öberg et al., 2011). The composition of the material accreted onto the planet during formation will reflect these differences. The C/O ratio in a HJs atmosphere would differ according to where it formed relative to the H<sub>2</sub>O, C and CO snow-lines. HJs formed in-situ would have compositions reflecting the inner disk, where there are few ices, and HJs involved in high eccentricity migration would have compositions that mirror the outer disk. HJs arriving through disk migration would be comprised of both outer and inner material if accretion occurred along the way (Alibert et al., 2005). Complications do arise when attempting to determine formation from atmospheric composition alone. Disk conditions influence the dynamics and chemistry within the disk which can then change the location of the ice lines (Piso et al., 2015) and planetesimals can contribute to the planet’s overall atmospheric composition (Sing et al. 2016).

### Clear Atmospheres

HJs that have observably clear atmospheres seem to be rare, making up close to 7% of cases, and are of very high value to the field (Wakeford et al. 2019). These HJs (e.g., WASP 96b (Nikolov et al. 2018) and WASP 39b (Nikolov et al. 2016; Fischer et al. 2016; Wakeford et al. 2018; Kirk et al. 2019), HD 209458b and WASP 17b) have had great success in constraining H<sub>2</sub>O and Na abundances and atmospheric metallicity. Probing clear atmospheres with low-resolution transit spectroscopy offers a unique opportunity to gain valuable atmospheric chemistry insights. Observing in the near-UV and looking for a detection of a Rayleigh scattering slope defines the hydrogen continuum level and would prove that the planet has a clear atmosphere at the limb (e.g., Fraine et al. 2014; Kreidberg et al. 2014; Sing et al. 2016; Kilpatrick et al. 2018).

### Aerosols

With respect to transmission spectroscopy in the optical and near-IR, clouds are defined as large particles that act as gray scatterers/absorbers, and hazes are defined as small particles that preferentially scatter visible short wavelength light (Pont et al., 2008; Sing et al., 2016; Barstow et al., 2017; Goyal et al., 2018). Hazes form directly from energy input via high energy particle bombardment or photochemistry whereas clouds are formed from gases originating through photochemistry. The term aerosols is generally used in the literature to describe both cloud/haze particles. They can produce muted spectral features of prominent chemical species (Deming et al., 2013) and optical spectral slopes that are not in alignment with gaseous Rayleigh scattering (Pont et al., 2013; Line and Parmentier, 2016). Both the formation and distribution of aerosols are directly related to the thermal structure and overall composition of the exoplanetary atmosphere.

Figure 15 presents transmission spectra of several exoplanets, showing how aerosols can impact the observed size of the exoplanet as a function of the observed wavelength. HJ HD 189733b’s spectra stands out in the figure as it’s atmosphere is dominated by strong Rayleigh scattering in the entire visible range (0.4 - 0.7  $\mu\text{m}$ ) and into the infrared (Pont et al., 2013). Heng (2016) measured the amplitudes of the Na and K absorption peaks (shown in the figure as vertical black dashed lines) at optical wavelengths and found that higher equilibrium temperature planets tended to be clearer than their counterparts.

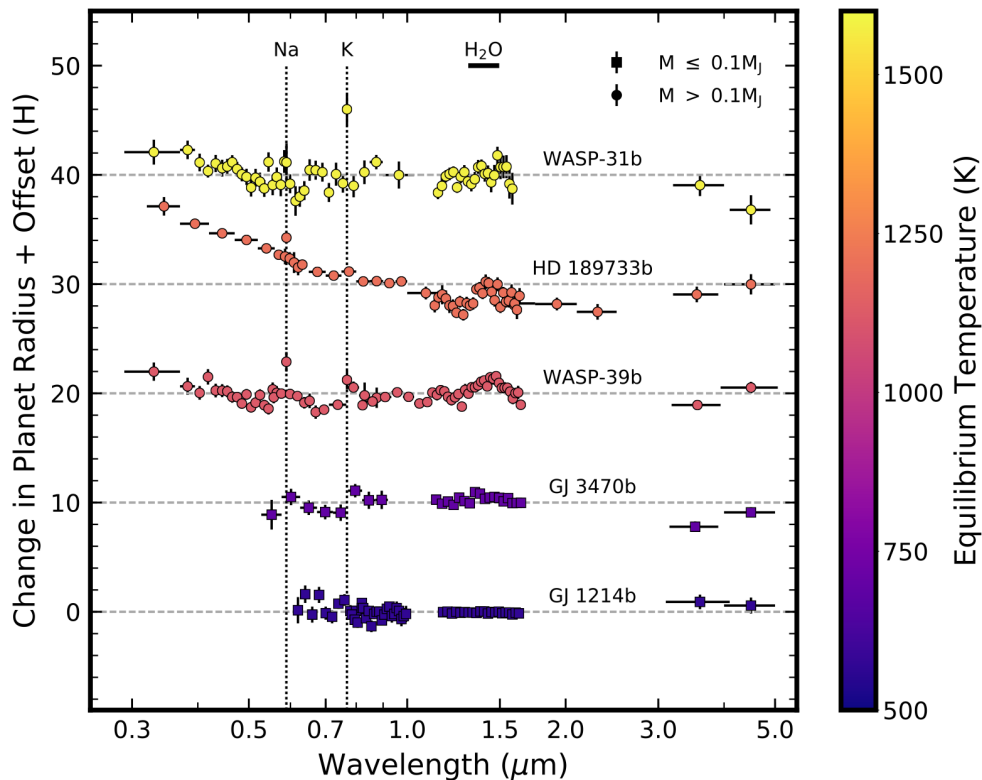


Figure 15: Impact of aerosols on the transmission spectra of selected exoplanets. The circles indicate planets that have  $>0.1 M_J$  and the square are the remaining lower mass planets. The colors of each of the data sets indicate the planet’s equilibrium temperature. Each spectra is offset for clarity, displayed in planetary scale heights, and normalized to the mean transit depth. Image credit: (Gao et al., 2021)

Exoplanet aerosol models predict that aerosols are likely composed of oxidized minerals (i.e., silicates) for the hottest planets and alkali salts and sulfides in the lower temperature planets (Gao et al. 2021). A great

deal of work is still necessary in this area as this type of modelling is highly complex. New ground and spaced based observations will help us gain more insights as to the composition of exoplanet aerosols while modelling and laboratory work will aid in understanding their formation and dynamics.

### Atmospheric Dynamics

Circulation patterns in the atmospheres of HJs have been studied in greater detail than ever before due to advancements in observation techniques. Studies using thermal phase curves (Zhang et al., 2018), measuring of wind speeds (Snellen et al., 2010), and eclipse mapping (de Wit et al., 2012) have been promising. For highly irradiated HJs, there is general agreement that there exists a trend with lower energy circulation efficiencies and increasing irradiation. For example, with higher equilibrium temperatures there is an increase in the contrasting day-night side temperatures. They also point out that in most of the HJ thermal phase curves, the hot spot in the atmosphere on the day-side is shifted slightly downwind. This is in agreement with General Circulation Models as it is away from the sub-stellar point ((e.g., Kilpatrick et al., 2018).

### Atmospheric Escape

Strong detections of atomic species in the atmospheres of giant, transiting exoplanets have been confirmed with transmission spectra observations done in the UV (e.g., Vidal-Madjar et al., 2003). Absorption by Lyman-alpha in the UV has shown H in the exosphere in many HJs (Bourrier et al., 2013; Ehrenreich et al., 2015). These observations aid in constraining hydro-dynamical escape processes, the morphology of the escaping cloud, and mass loss rates (see Owen, 2018 for a detailed review). There are two emerging consensus to be noted. The first is that highly irradiated Neptune-sized exoplanets orbiting low mass stars are excellent targets for atmospheric escape studies (Ehrenreich et al., 2015; Bourrier et al., 2018). While the planet and its escaping atmosphere are transiting the star, the observed transit would show the mass loss signature - appearing deeper and longer in the UV than in the optical. Both HJs and lower-mass exoplanets experience atmospheric escape but for HJs the mass loss is not substantial enough to affect their evolution. For the smaller planets, this atmospheric escape drives their evolution. Secondly, new observations of He in the IR are opening new pathways to investigate exoplanet exospheres from both the ground and from space (Spake et al., 2018; Allart et al., 2018).

### Temperatures

Obtaining planetary equilibrium temperature is practical for making comparisons of planets in different temperature regimes, but it is not useful in drawing any conclusions about their climate (Leconte et al. 2013). Temperatures on the surface of the planet are driven by the complex interaction between greenhouse effects and planetary albedo and are not currently possible to directly measure. A planets albedo can be determined from the planet/star flux ratios or through equilibrium temperatures found by spectroscopic observations (Cowan et al. 2012, Cowan & Agol 2011). Alternatively, the equilibrium temperature can be inferred from the planetary albedo using photometry from the thermal and optical phase curve (Mallama 2009; von Paris et al. 2016)

Thermal emission spectra provide the equilibrium temperature (thus pressure/altitude corresponding to the photosphere) as a function of wavelength in the atmosphere of the exoplanet. These create the important pressure-temperature (P-T) profiles that bring understanding to the radiative processes and their relationship with the dynamical and chemical processes in the atmospheres (see Madhusudhan 2018 for a review). There are three broad P-T profiles observed in HJs; isothermal profiles, profiles with no thermal inversions, and profiles with thermal inversions (see again the left side of Figure 14). Most HJs fall into the category of no thermal inversions with thermal inversions limited to irradiated ultra-HJs with temperatures  $\leq 2500$  K (Sheppard et al., 2017; Evans et al., 2017; Haynes et al., 2015). These types of exoplanets provide excellent testing grounds for thermal inversion studies.

The *equilibrium temperature* ( $T_{eq}$ ) can be calculated as the theoretical temperature of a planet assuming it is a blackbody being heated solely by its host star and neglects effects of a potential atmosphere (i.e., greenhouse effects, albedo). The *effective temperature* ( $T_{eff}$ ) of an object would be the temperature of a blackbody that emits the same total electromagnetic radiation or has an identical peak wavelength. Stars are close to being perfect blackbodies and planets can be approximated as such. A blackbody an idealized object that absorbs every type of incident radiation upon it. When a blackbody is in thermal equilibrium it emits blackbody radiation, which correlates to both the objects temperature and its peak/max wavelength. Wien's Displacement Law describes this relationship:

$$\lambda_{max}[m] = \frac{b}{T}, \quad (21)$$

where the constant  $b = 2.9 \times 10^{-3} \text{m K}$ , and T is the temperature. Thermal equilibrium implies that incident radiation is equivalent to emitted radiation. The radiation from the blackbody is describes by the Planck Function in both frequency units

$$B_\nu(T) [\text{erg s}^{-1} \text{ cm}^{-2} \text{ Hz}^{-1} \text{ sr}^{-1}] = \frac{2h\nu^3/c^2}{e^{h\nu/kT} - 1} \quad (22)$$

and wavelength units

$$B_\lambda(T) [\text{erg s}^{-1} \text{ cm}^{-3} \text{ sr}^{-1}] = \frac{2hc^2/\lambda^5}{e^{hc/\lambda kT} - 1}. \quad (23)$$

If we wanted to find the total power output at a specified frequency or wavelength, we would need to solve for the *monochromatic luminosity* ( $L_\lambda d\lambda$ ). This can be found by integrating the Planck Function over the surface area of the sphere and all solid angle in a hemisphere:

$$L_\lambda d\lambda [\text{erg s}^{-1} \text{ cm}^{-1}] = 4\pi^2 R^2 B_\lambda d\lambda. \quad (24)$$

Now, the *luminosity* can be found by integrating  $L_\lambda(T)d\lambda$  over the all wavelengths:

$$L [\text{erg s}^{-1}] = 4\pi R^2 \sigma T^4, \quad (25)$$

where  $\sigma$  is the Stefan-Boltzmann constant. This relation can be re-arranged to solve for the effective temperature:

$$T_{\text{eff}} [K] = \left[ \frac{L}{4\pi R^2 \sigma} \right]^{1/4}. \quad (26)$$

Consider an orbiting planet at a distance  $d$  from the star with a radius  $R_p$ . The energy flux,  $F$ , received by the planet can be written:

$$F [\text{erg m}^2 \text{ s}^{-1}] = \frac{L_*}{4\pi d^2} = \frac{4\pi R_*^2 \sigma T_*^4}{4\pi d^2} \quad (27)$$

Now the power received by the planet can be found as:

$$P_{\text{in}} = \frac{L_*}{4\pi d^2} (\pi R_p^2) (1 - A_b) = 4\pi R_*^2 \sigma T_*^4 \left[ \frac{\pi R_p^2}{4\pi d^2} \right] (1 - A_b), \quad (28)$$

where  $A_b$  is the *bond albedo*, or fraction of the light that is reflected from the planet. If the planet is approximated as a blackbody then the condition of equilibrium implies the power in equals the power out ( $P_{\text{in}} = P_{\text{out}}$ ). Invoking the Stefan-Boltzmann equation for the planet gives

$$P_{\text{out}} = 4\pi R_p^2 \sigma T_p^4, \quad (29)$$

and solving for  $T_p$  with Equations 28 and 29 gives

$$T_p = T_{\text{eq}} = T_* \sqrt{\frac{R_*}{2d}} (1 - A_b)^{1/4}. \quad (30)$$

In addition, there is an *irradiation temperature*,

$$T_{\text{irr}} = T_{\text{eff}} \sqrt{\frac{R_*}{a}} \quad (31)$$

Little is known about the albedos of exoplanets. The majority of measurements done to date are from HJs ( $T_{\text{eq}} > 1000$  K and  $R_p \sim R_J$  and have shown low albedos of  $A_b \leq 0.2$ . Exceptions exist where there are higher albedos which indicate the presence of highly reflective clouds.

## 4 Thesis Proposal

### 4.1 Scope of Work

With my thesis, I propose to investigate the nature of transiting HJ atmospheres with low-resolution, multi-broadband transit photometry observations from the Wyoming Infrared Observatory (WIRO). HJs give the best chance for detecting an atmospheric signal due to their large transit depths and inflated radii. The main exoplanet atmospheric features revealed by HST spectroscopy are broadband components. Thus, low-resolution photometry from the ground can provide valuable constraints on the architecture and composition of these planets (Bento et al., 2014) (Nascimbeni et al., 2013). This type of work is relevant to the pursuit of vetting and selecting interesting exoplanets for more detailed follow-up observations using space-based observatories (i.e., JWST, HST). My proposed work encompasses the following open questions and priorities in the field:

- **Investigate whether Super Rayleigh Slopes (SRS) are preferential to HJs with hazy atmospheres/specific equilibrium temperatures.** It is theorized that the spectral slope is significantly enhanced by haze when the eddy diffusion dominates over the settling of haze particles in the atmosphere (Ohono et al. 2020). The equilibrium temperature of the exoplanet is associated with the coefficient that describes eddy diffusion (Komacek et al. 2019):

$$\log_{10}(K_z[m^2s^{-1}]) = 2.110 \left( \frac{T_{eq}}{1000K} \right) + 1.855. \quad (32)$$

Theoretically, a preferred equilibrium temperature ( $T_{eq} \sim 1000\text{--}1500$  K) may exist for haze preferentially producing SRSs. In retrieval results from Ohono et al. (2020), planets with  $T_{eq}$  of  $\sim 1200\text{--}1400$  K tend to exhibit the steep spectral slopes that resemble the haze-generated SRSs. Preliminary evidence suggests that hotter planets are more likely to have cloud-free atmospheres when compared to their cooler counterparts (e.g., Stevenson 2016; Heng 2016; Fu et al. 2017; Crossfield & Kreidberg 2017; Evans et al. 2018; Hoeijmakers et al. 2018, 2019) [I will measure the spectral slopes of HJs over a wide range of  \$T\_{eq}\$  \(950 K >  \$T\_{eq}\$  > 4020 K\) to investigate whether exoplanets with SRSs are predominantly the result of atmospheric haze.](#)

- **Investigate the transmission spectra of HJs with various surface gravity and stellar activity for evidence of SRSs.** Only few exoplanets with intermediate  $g$  values ( $\sim 25\text{ m s}^{-2}$ ) have their transmission spectrum measured. The current sample of intermediate gravity exoplanets tends to display SRSs, such as HD 189733b ( $21.5\text{ m s}^{-2}$ ; Sing et al. 2011; Pont et al. 2013), TrES-3b ( $27.4\text{ m s}^{-2}$ ; Parviainen et al. 2016), and WASP 43b ( $47\text{ m s}^{-2}$ ; Weaver et al. 2020). Low-gravity ( $\leq 15\text{ m s}^{-2}$ ) HJs have also been observed to have steep scattering slopes, such as WASP 121b ( $9.4\text{ m s}^{-2}$ ; Evans et al. 2018). There is much debate as to whether potential spot contamination induced by the host star is the underlying physical mechanism responsible for the SRS, including HD 189733b (McCullough et al. 2014), WASP 43b (Weaver et al. 2020), and WASP 19b (Espinoza et al. 2019). If not known, stellar activity must be accurately characterized, as faculae and spots can mimic planetary atmosphere absorption features (e.g., Oshagh et al. 2014; McCullough et al. 2014; Kirk et al. 2016; Rackham et al. 2017; Cauley et al. 2018). [With targets spanning the range of low to very high surface gravity \( \$\sim 5\text{--}100\text{ m s}^{-2}\$ \), I aim to shed light on the underlying mystery of SRSs with respect to planetary surface gravity and stellar activity.](#)
- **Determine if WIRO is capable of detecting the Na absorption feature in HJ atmospheres with a broadband filter.** Broad absorption features of the Na I and K I resonance doublets have long been theorized in the optical spectra of irradiated cloud-free HJs (e.g., Seager & Sasselov 2000; Sudarsky et al. 2000; Burrows et al. 2000). Haze and clouds in the atmospheres are believed to be responsible for obscuring the broad absorption feature (e.g., Charbonneau et al. 2002; Sing et al. 2016). Figure 1 from Nikolov et al. (2018) shows that the precision necessary to detect the core of the Na absorption line is  $\sim 4000$  parts-per-million (ppm). Although a high-resolution detection of the broad absorption wings remain out of reach, WIRO may be capable of reaching the precision necessary for a low-resolution core detection of Na ( $0.59\mu\text{m}$ ) within the Sloan  $r$  broadband. This detection may be observed as an enhanced radius ratio in the  $r$  band in comparison to the adjoining  $g$  and  $i$  bands. [I will demonstrate the capabilities of WIRO in the detection of the important Na absorption feature from a 2.3m ground-based observatory.](#)
- **Perform a multi-year ground-based observing campaign.** Observing the optical transmission spectrum is fundamental in furthering our understanding of exoplanetary atmospheres as it is needed to provide constraints on abundances that have been derived from infrared data (e.g., Benneke & Seager 2012; Heng & Kitzmann 2017; Wakeford et al. 2018; Pinhas et al. 2019). With only  $\sim 50$  exoplanets observed in this detail, the number of planets with an observed transmission spectrum must increase to gain a better understanding of the diversity of clear to cloudy atmospheres (e.g., Lecavelier Des Etangs et al. 2008a,b; Sing et al. 2011; Kirk et al. 2017; Mallonn & Wakeford 2017). Having a better understanding of exoplanetary system parameters is invaluable to predicting whether a planet is more likely to have a clear or cloudy atmosphere (e.g., stellar metallicity,  $T_{eq}$ ,  $g$ ). [By the end of my time as a doctoral student at UWt his project will have amassed transmission spectra of transiting planets over the summer months of 2020-2022. In the 2020 observing campaign alone, we were able to observe over 25 known and TESS candidate planets more than once. This quality of data set is both timely and invaluable to the exoplanetary community.](#)

## 4.2 Photometric Requirements

The precision necessary to measure a changing  $R_p/R_*$  over multiple bandpasses approaches several hundred parts-per-million (ppm). Observations from space do this precision and better because they offer ideal photometric conditions – where there is no interference from Earth’s atmosphere. Kasper et al. (2019) has shown

that WIRO is capable of detecting variations in  $R_p/R_*$  over the *urgiz* broadbands to a precision of several hundred ppm. Various upgrades to both the telescope optics (light diffuser) and observing methods (i.e, tracking, observing target and field on the same pixels during each transit event) have improved the precision to  $\sim 60$  ppm for our best targets. **We are observing with space-like photometric precision from the ground.** Figure 16 shows the *AstroImageJ* undetrended and fitted lightcurve for Kelt-23Ab from the night of August, 9 2020 with various sky/detector parameters plotted beneath it. The root-mean-square (RMS), or uncertainty, in the transit data mis calculated as as 66 ppm. To achieve the highest precision, the best approach is to repeatedly observe the transit, implement differential photometry, and robustly detrend the data (and, of course, have beautifully photometric nights!).

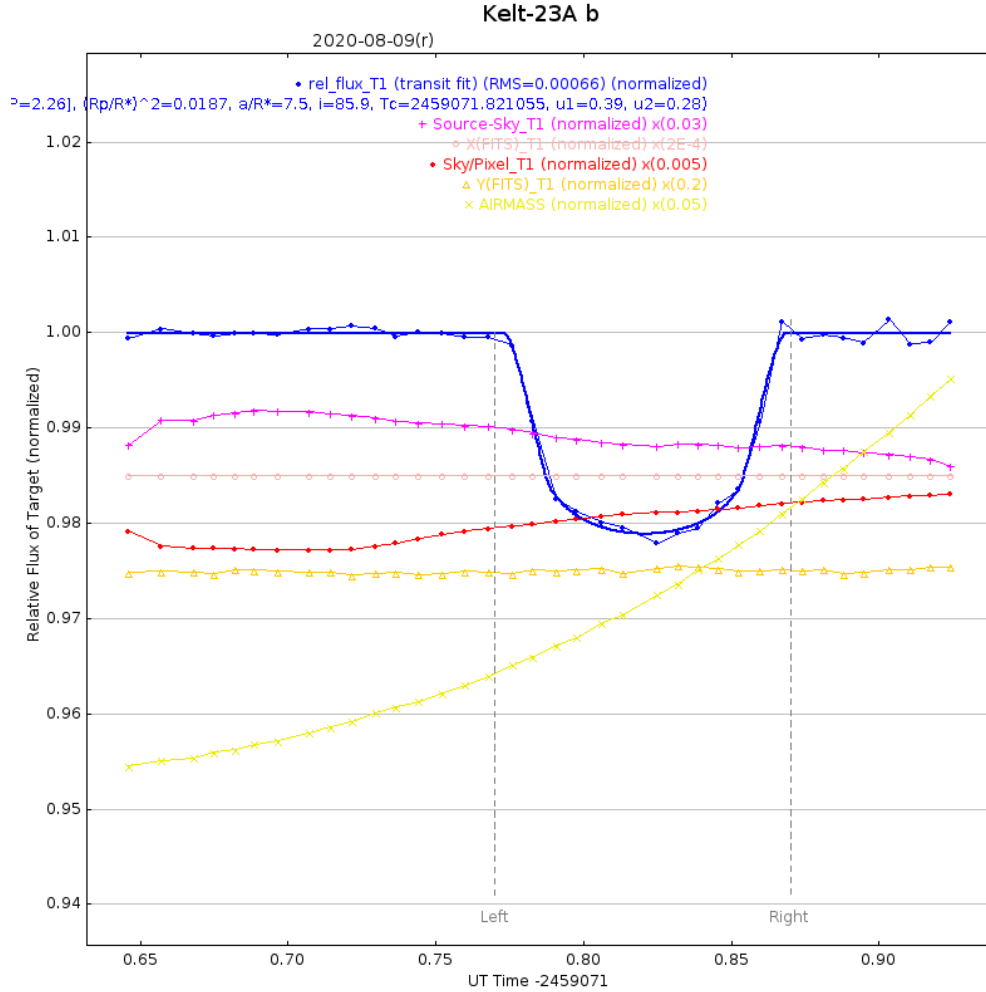


Figure 16: Undetrended and fitted lightcurve of Kelt-23Ab. The RMS value gives us an estimation of our uncertainty in the transit data.

#### 4.2.1 Signal to Noise Calculations

The source and sky are respectively the two most dominant sources of noise in this ground-based observing program. A quick signal to noise estimation can be done assuming a source noise dominated observation and neglecting other sources of noise. These other detector and non-detector sources include: flat-fielding, bias, dark current, sky noise (i.e., Earth’s atmosphere, the Moon, satellites), and host star stellar jitter (i.e., flares, spots, pulses). This estimation is important in determining before-hand what targets will be the most beneficial to observe. Figure 17 looks at the signal-to-noise ratio (SNR) as a function of  $R_p/R_*$ . The larger the  $R_p/R_*$ , the lower the SNR needed to detect the transit. Detection of smaller planets to the  $10\sigma$  level are possible to sizes down to about Neptune. Earth-sized planets are not shown on this plot as they require SNRs that are beyond our abilities at this time.

Figure 18 illustrates the minimum signal to noise needed to detect an atmosphere around a transiting  $1 R_J$  exoplanet. I stress minimum here because this is neglecting other sources of noise. The atmosphere is depicted in the plot as the variation in apparent radii difference in red to blue wavelengths (typical of Rayleigh

scattering) on the order of 1-10%. The larger the atmosphere, the easier it is to collect the photons necessary for a detection. Note that a percent difference of 10% is extremely optimistic. The maximum signal to noise obtained with WIRO using the optical diffuser is highlighted by the dashed line. Given that this is also the lower limit of the SNR estimation, the best hope for a confident atmospheric detection is minimal sky noise and a large exoplanet atmosphere.

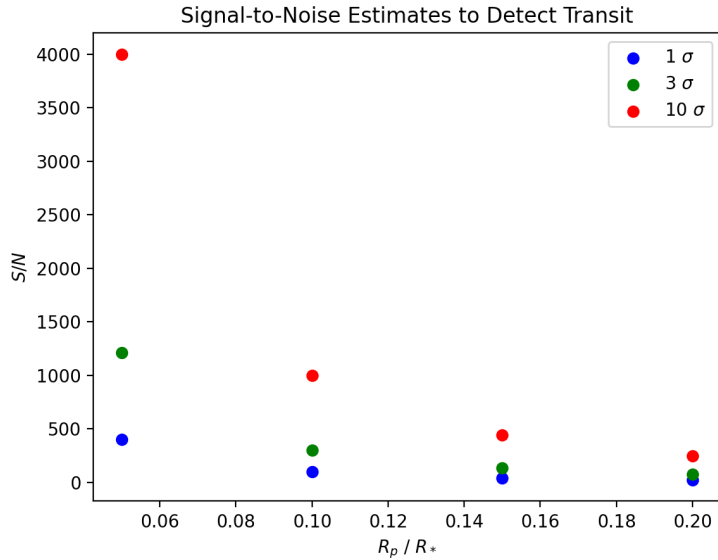


Figure 17: Signal to noise estimations of the detection of various sized (from Neptune to 2 Jupiter-radii) exoplanets transiting a Sun-type star.

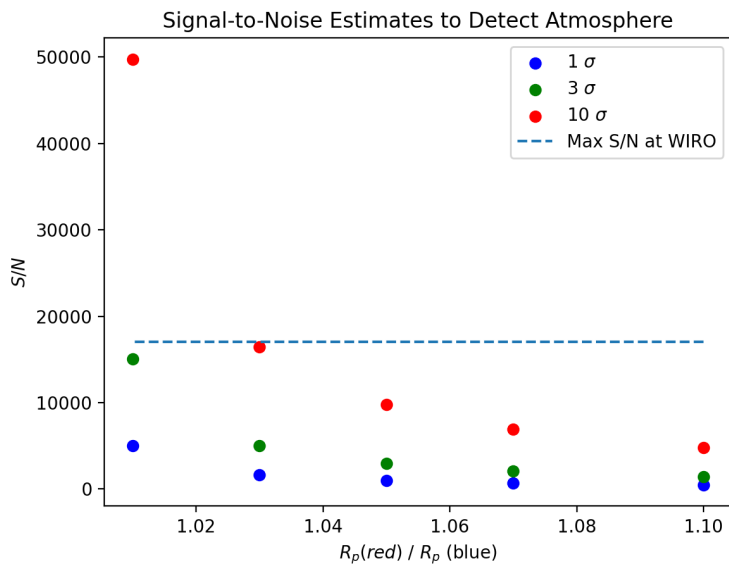


Figure 18: Signal to noise estimation of the detection of an atmosphere around a  $1 R_J$  exoplanet (around a Sun-type star) whose apparent radius in red to blue wavelengths varies from 1-10%. This extremely optimistic calculation only takes into account photon noise and ignores the non-negligible and unpredictable sky noise. The maximum signal to noise with the WIRO diffuser is shown with the dashed line at approximately  $S/N \approx 17,000$ .

Consider a Jupiter-sized planet transiting a Sun-like star, where  $R_p/R_*=0.1$  and a ratio of the intensity in and out of transit ( $I_{min}/I_{max}$ ) is 0.99. In order to detect the transit signal the SNR must be 100:1 as the intensity varies on the 1% level. The standard assumption made is that the target resides in the Poisson limit or is photon noise dominated because the counts occur at a constant mean rate and are independent of the time of the previous event (Haight, 1967). To good approximation, we describe the SNR as:

$$SNR = \sqrt{N_{\text{target}}} \rightarrow N_{\text{photons}} = 100^2 = 10^4 \quad (33)$$

where  $N_{\text{target}}$  is the total number of photons collected from the target during the exposure. To detect the Jupiter-sized planet in our example, our detector would need to collect  $10^4$  photons from the source. This example demonstrates the minimum amount of photons needed to make a  $1\sigma$  detection at 1%. For a  $3\sigma$  detection at 1%,  $SNR = 300:1$  and  $N_{\text{photons}} = 90,000$ . For a  $10\sigma$  detection at 1%,  $SNR = 1000:1$  and  $N_{\text{photons}} = 10^6$ . A problem arises here because modern detectors are only able to hold about 100,000 photons per pixel. Clever techniques are implemented to spread the incoming light onto more pixels and therefore collect many more photons. One method is to defocus the telescope (see Kasper et al. (2019) for this technique implemented at WIRO) and another is to use a beam shaping diffuser (this work). Figures 19 and 20 show the point-spread-functions (PSFs) of a defocused star and a diffused star taken from WIRO. The defocused star shows a doughnut shaped PSF and is highly variable in time. Diffusers greatly improve the photometry due to their molding of the star's PSF into a stable and broad top-hat shape which minimizes error from variable pixel response, seeing effects from the atmosphere, imperfect telescope guiding, and telescope induced aberrations on the image as seen by defocusing (Stefansson et al., 2017). WIRO's diffuser, generously loaned from Penn State, is able to spread light over a circular aperture of  $\approx 3900$  pixels. At 100,000 photons per pixel, the 3900 pixels can collectively gather  $3.9 \times 10^8$  photons. The  $\sigma_{\text{target}}$  that can be achieved at this level is:

$$\sigma_{\text{target}} = \sqrt{3.9 \times 10^8 \text{ photons}} \approx 19,700, \quad (34)$$

or 51 ppm (parts per million). The error on this measurement would be  $51/10^6 = 0.000051$  (0.0051%). At this level of precision, an atmosphere around a HJ is detectable. We are achieving values very close to this!

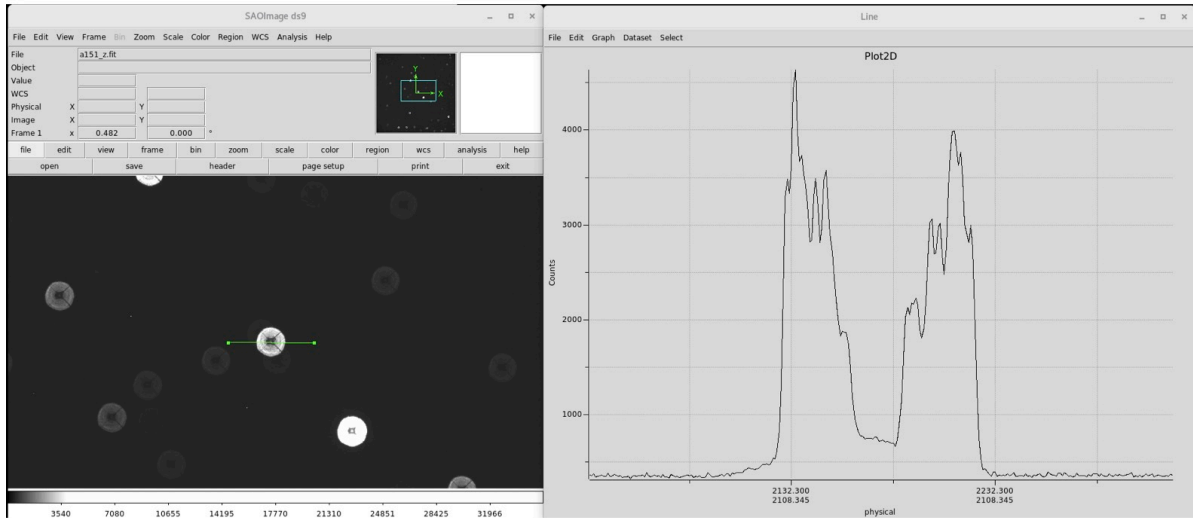


Figure 19: *Left*: Raw image of a defocused star on the left in the *Ds9* astronomical imaging software. *Right*: The corresponding PSF from the green line cut through the center on the right.

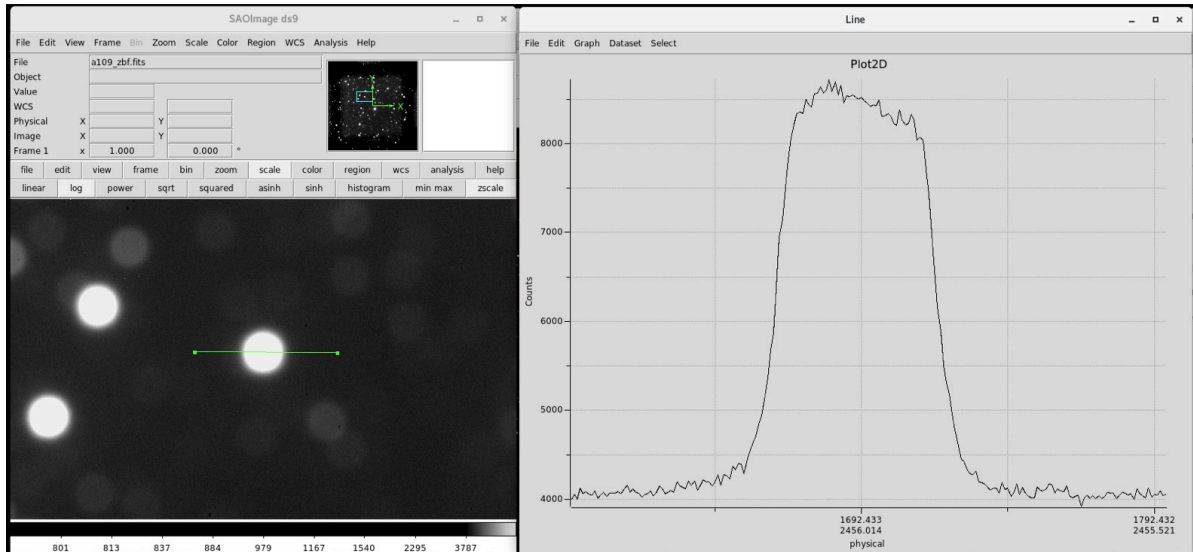


Figure 20: Raw image of a diffused star on the left in the *Ds9* astronomical imaging software. *Right*: The corresponding PSF from the green line cut through the center on the right. .

## 5 Appendix

WIRO Information	
Latitude	41.09705
Longitude	-105.977103
Altitude (m)	2935
Aperture (m)	2.3368
Effective f Ratio	2.3
Focal Length (mm)	5374.64
Plate Scale "/mm	38.38

WIRO DoublePrime Specifications	
Pixel Size ( $\mu\text{m}$ )	15
Naxis1	4096
Naxis2	4096
Arcsec/Pixel	0.576
FOV1 (arcmin)	39.3
FOV2 (arcmin)	39.3
Sensor Temp (C)	-110
Gain (e-/ADU)	2.6
Read Noise (e-)	5.2
Dark Noise (e-/s/pix)	0.003

## References

- Agol, E., Steffen, J., Sari, R., and Clarkson, W. (2005). On detecting terrestrial planets with timing of giant planet transits. , 359(2):567–579.
- Akeson, R. L., Chen, X., Ciardi, D., Crane, M., Good, J., Harbut, M., Jackson, E., Kane, S. R., Laity, A. C., Leifer, S., Lynn, M., McElroy, D. L., Papin, M., Plavchan, P., Ramírez, S. V., Rey, R., von Braun, K., Wittman, M., Abajian, M., Ali, B., Beichman, C., Beekley, A., Berriman, G. B., Berukoff, S., Bryden, G., Chan, B., Groom, S., Lau, C., Payne, A. N., Regelson, M., Saucedo, M., Schmitz, M., Stauffer, J., Wyatt, P., and Zhang, A. (2013). The NASA Exoplanet Archive: Data and Tools for Exoplanet Research. , 125(930):989.
- Alibert, Y., Mordasini, C., Benz, W., and Winisdoerffer, C. (2005). Models of giant planet formation with migration and disc evolution. , 434(1):343–353.
- Allart, R., Bourrier, V., Lovis, C., Ehrenreich, D., Spake, J. J., Wyttenbach, A., Pino, L., Pepe, F., Sing, D. K., and Lecavelier des Etangs, A. (2018). Spectrally resolved helium absorption from the extended atmosphere of a warm Neptune-mass exoplanet. *Science*, 362(6421):1384–1387.
- Alonso, R., Brown, T. M., Charbonneau, D., Dunham, E. W., Belmonte, J. A., Deeg, H. J., Fernández, J. M., Latham, D. W., Mandushev, G., O’Donovan, F. T., Rabus, M., and Torres, G. (2007). The Transatlantic Exoplanet Survey (TrES): A Review. In Afonso, C., Weldrake, D., and Henning, T., editors, *Transiting Extrapolar Planets Workshop*, volume 366 of *Astronomical Society of the Pacific Conference Series*, page 13.
- Baraffe, I., Chabrier, G., and Barman, T. (2010). The physical properties of extra-solar planets. *Reports on Progress in Physics*, 73(1):016901.
- Batygin, K., Bodenheimer, P. H., and Laughlin, G. P. (2016). In Situ Formation and Dynamical Evolution of Hot Jupiter Systems. , 829(2):114.
- Bell, T. J. and Cowan, N. B. (2018). Increased Heat Transport in Ultra-hot Jupiter Atmospheres through H<sub>2</sub> Dissociation and Recombination. , 857(2):L20.
- Bento, J., Wheatley, P. J., Copperwheat, C. M., Fortney, J. J., Dhillon, V. S., Hickman, R., Littlefair, S. P., Marsh, T. R., Parsons, S. G., and Southworth, J. (2014). Optical transmission photometry of the highly inflated exoplanet WASP-17b. , 437(2):1511–1518.
- Boley, A. C., Granados Contreras, A. P., and Gladman, B. (2016). The In Situ Formation of Giant Planets at Short Orbital Periods. , 817(2):L17.
- Bond, I. A., Bennett, D. P., Sumi, T., Udalski, A., Suzuki, D., Rattenbury, N. J., Bozza, V., Koshimoto, N., Abe, F., Asakura, Y., Barry, R. K., Bhattacharya, A., Donachie, M., Evans, P., Fukui, A., Hirao, Y., Itow, Y., Li, M. C. A., Ling, C. H., Masuda, K., Matsubara, Y., Muraki, Y., Nagakane, M., Ohnishi, K., Ranc, C., Saito, T., Sharan, A., Sullivan, D. J., Tristram, P. J., Yamada, T., Yamada, T., Yonehara, A., Skowron, J., Szymański, M. K., Poleski, R., Mróz, P., Soszyński, I., Pietrukowicz, P., Kozłowski, S., Ulaczyk, K., and Pawlak, M. (2017). The lowest mass ratio planetary microlens: OGLE 2016-BLG-1195Lb. , 469(2):2434–2440.
- Bond, I. A., Udalski, A., Jaroszyński, M., Rattenbury, N. J., Paczyński, B., Soszyński, I., Wyrzykowski, L., Szymański, M. K., Kubiak, M., Szewczyk, O., Żebruń, K., Pietrzyński, G., Abe, F., Bennett, D. P., Eguchi, S., Furuta, Y., Hearnshaw, J. B., Kamiya, K., Kilmartin, P. M., Kurata, Y., Masuda, K., Matsubara, Y., Muraki, Y., Noda, S., Okajima, K., Sako, T., Sekiguchi, T., Sullivan, D. J., Sumi, T., Tristram, P. J., Yanagisawa, T., Yock, P. C. M., and OGLE Collaboration (2004). OGLE 2003-BLG-235/MOA 2003-BLG-53: A Planetary Microlensing Event. , 606(2):L155–L158.
- Bonfils, X., Delfosse, X., Udry, S., Forveille, T., Mayor, M., Perrier, C., Bouchy, F., Gillon, M., Lovis, C., Pepe, F., Queloz, D., Santos, N. C., Ségransan, D., and Bertaux, J. L. (2013). The HARPS search for southern extra-solar planets. XXXI. The M-dwarf sample. , 549:A109.
- Borucki, W. J., Koch, D., Basri, G., Batalha, N., Brown, T., Caldwell, D., Caldwell, J., Christensen-Dalsgaard, J., Cochran, W. D., DeVore, E., Dunham, E. W., Dupree, A. K., Gautier, T. N., Geary, J. C., Gilliland, R., Gould, A., Howell, S. B., Jenkins, J. M., Kondo, Y., Latham, D. W., Marcy, G. W., Meibom, S., Kjeldsen, H., Lissauer, J. J., Monet, D. G., Morrison, D., Sasselov, D., Tarter, J., Boss, A., Brownlee, D., Owen, T., Buzasi, D., Charbonneau, D., Doyle, L., Fortney, J., Ford, E. B., Holman, M. J., Seager, S., Steffen, J. H., Welsh, W. F., Rowe, J., Anderson, H., Buchhave, L., Ciardi, D., Walkowicz, L., Sherry, W., Horch, E., Isaacson, H., Everett, M. E., Fischer, D., Torres, G., Johnson, J. A., Endl, M., MacQueen, P., Bryson, S. T., Dotson, J., Haas, M., Kolodziejczak, J., Van Cleve, J., Chandrasekaran, H., Twicken, J. D., Quintana, E. V., Clarke, B. D., Allen, C., Li, J., Wu, H., Tenenbaum, P., Verner, E., Bruhweiler, F., Barnes, J., and Prsa, A. (2010). Kepler Planet-Detection Mission: Introduction and First Results. *Science*, 327(5968):977.

- Bourrier, V., Lecavelier des Etangs, A., Dupuy, H., Ehrenreich, D., Vidal-Madjar, A., Hébrard, G., Ballester, G. E., Désert, J. M., Ferlet, R., Sing, D. K., and Wheatley, P. J. (2013). Atmospheric escape from HD 189733b observed in H I Lyman- $\alpha$ : detailed analysis of HST/STIS September 2011 observations. , 551:A63.
- Bourrier, V., Lecavelier des Etangs, A., Ehrenreich, D., Sanz-Forcada, J., Allart, R., Ballester, G. E., Buchhave, L. A., Cohen, O., Deming, D., Evans, T. M., García Muñoz, A., Henry, G. W., Kataria, T., Lavvas, P., Lewis, N., López-Morales, M., Marley, M., Sing, D. K., and Wakeford, H. R. (2018). Hubble PanCET: an extended upper atmosphere of neutral hydrogen around the warm Neptune GJ 3470b. , 620:A147.
- Brogi, M., Line, M., Bean, J., Désert, J. M., and Schwarz, H. (2017). A Framework to Combine Low- and High-resolution Spectroscopy for the Atmospheres of Transiting Exoplanets. , 839(1):L2.
- Brown, T. M., Charbonneau, D., Gilliland, R. L., Noyes, R. W., and Burrows, A. (2001). Hubble Space Telescope Time-Series Photometry of the Transiting Planet of HD 209458. , 552(2):699–709.
- Charbonneau, D., Brown, T. M., Latham, D. W., and Mayor, M. (2000). Detection of Planetary Transits Across a Sun-like Star. , 529(1):L45–L48.
- Charbonneau, D., Brown, T. M., Noyes, R. W., and Gilliland, R. L. (2002). Detection of an Extrasolar Planet Atmosphere. , 568(1):377–384.
- Claret, A. (2000). *VizieR Online Data Catalog: Non-linear limb-darkening law for LTE models (Claret, 2000)*. *VizieR Online Data Catalog*, pages J/A+A/363/1081.
- Claret, A. (2004). A new non-linear limb-darkening law for LTE stellar atmosphere models III. Sloan filters: Calculations for  $-5.0 \leq \log [M/H] \leq +1$ ,  $2000 \text{ K} \leq T_{eff} \leq 50\,000 \text{ K}$  at several surface gravities. , 428:1001–1005.
- Cloutier, R., Astudillo-Defru, N., Doyon, R., Bonfils, X., Almenara, J. M., Benneke, B., Bouchy, F., Delfosse, X., Ehrenreich, D., Forveille, T., Lovis, C., Mayor, M., Menou, K., Murgas, F., Pepe, F., Rowe, J., Santos, N. C., Udry, S., and Wünsche, A. (2017). Characterization of the K2-18 multi-planetary system with HARPS. A habitable zone super-Earth and discovery of a second, warm super-Earth on a non-coplanar orbit. , 608:A35.
- Czesla, S., Huber, K. F., Wolter, U., Schröter, S., and Schmitt, J. H. M. M. (2009). How stellar activity affects the size estimates of extrasolar planets. , 505(3):1277–1282.
- Dawson, R. I. and Johnson, J. A. (2018). Origins of Hot Jupiters. , 56:175–221.
- de Wit, J., Gillon, M., Demory, B. O., and Seager, S. (2012). Towards consistent mapping of distant worlds: secondary-eclipse scanning of the exoplanet HD 189733b. , 548:A128.
- de Wit, J., Wakeford, H. R., Gillon, M., Lewis, N. K., Valenti, J. A., Demory, B.-O., Burgasser, A. J., Burdanov, A., Delrez, L., Jehin, E., Lederer, S. M., Queloz, D., Triaud, A. H. M. J., and Van Grootel, V. (2016). A combined transmission spectrum of the Earth-sized exoplanets TRAPPIST-1 b and c. , 537(7618):69–72.
- Deming, D. (2018). Helium discovered in the tail of an exoplanet. , 557(7703):35–36.
- Deming, D., Wilkins, A., McCullough, P., Burrows, A., Fortney, J. J., Agol, E., Dobbs-Dixon, I., Madhusudhan, N., Crouzet, N., Desert, J.-M., Gilliland, R. L., Haynes, K., Knutson, H. A., Line, M., Magic, Z., Mandell, A. M., Ranjan, S., Charbonneau, D., Clampin, M., Seager, S., and Showman, A. P. (2013). Infrared Transmission Spectroscopy of the Exoplanets HD 209458b and XO-1b Using the Wide Field Camera-3 on the Hubble Space Telescope. , 774(2):95.
- Demory, B.-O. and Seager, S. (2011). Lack of Inflated Radii for Kepler Giant Planet Candidates Receiving Modest Stellar Irradiation. , 197(1):12.
- Durisen, R. H., Boss, A. P., Mayer, L., Nelson, A. F., Quinn, T., and Rice, W. K. M. (2007). Gravitational Instabilities in Gaseous Protoplanetary Disks and Implications for Giant Planet Formation. In Reipurth, B., Jewitt, D., and Keil, K., editors, *Protostars and Planets V*, page 607.
- Ehrenreich, D., Bourrier, V., Wheatley, P. J., Lecavelier des Etangs, A., Hébrard, G., Udry, S., Bonfils, X., Delfosse, X., Désert, J.-M., Sing, D. K., and Vidal-Madjar, A. (2015). A giant comet-like cloud of hydrogen escaping the warm Neptune-mass exoplanet GJ 436b. , 522(7557):459–461.
- Evans, T. M., Sing, D. K., Kataria, T., Goyal, J., Nikolov, N., Wakeford, H. R., Deming, D., Marley, M. S., Amundsen, D. S., Ballester, G. E., Barstow, J. K., Ben-Jaffel, L., Bourrier, V., Buchhave, L. A., Cohen, O., Ehrenreich, D., García Muñoz, A., Henry, G. W., Knutson, H., Lavvas, P., Lecavelier Des Etangs, A., Lewis, N. K., López-Morales, M., Mandell, A. M., Sanz-Forcada, J., Tremblin, P., and Lupu, R. (2017). An ultrahot gas-giant exoplanet with a stratosphere. , 548(7665):58–61.

- Fernandes, R. B., Mulders, G. D., Pascucci, I., Mordasini, C., and Emsenhuber, A. (2019). Hints for a Turnover at the Snow Line in the Giant Planet Occurrence Rate. , 874(1):81.
- Ford, E. B. (2014). Architectures of planetary systems and implications for their formation. *Proceedings of the National Academy of Science*, 111(35):12616–12621.
- Fortney, J. J., Dawson, R. I., and Komacek, T. D. (2021). Hot Jupiters: Origins, Structure, Atmospheres. *arXiv e-prints*, page arXiv:2102.05064.
- Fortney, J. J., Marley, M. S., Lodders, K., Saumon, D., and Freedman, R. (2005). Comparative Planetary Atmospheres: Models of TrES-1 and HD 209458b. , 627(1):L69–L72.
- Fossati, L., Haswell, C. A., Froning, C. S., Hebb, L., Holmes, S., Kolb, U., Helling, C., Carter, A., Wheatley, P., Collier Cameron, A., Loeillet, B., Pollacco, D., Street, R., Stempels, H. C., Simpson, E., Udry, S., Joshi, Y. C., West, R. G., Skillen, I., and Wilson, D. (2010). Metals in the Exosphere of the Highly Irradiated Planet WASP-12b. , 714(2):L222–L227.
- Gao, P., Wakeford, H. R., Moran, S. E., and Parmentier, V. (2021). Aerosols in Exoplanet Atmospheres. *arXiv e-prints*, page arXiv:2102.03480.
- Gaudi, B. S., Christiansen, J. L., and Meyer, M. R. (2020). The Demographics of Exoplanets. *arXiv e-prints*, page arXiv:2011.04703.
- Gibson, N. P., Aigrain, S., Barstow, J. K., Evans, T. M., Fletcher, L. N., and Irwin, P. G. J. (2013). The optical transmission spectrum of the hot Jupiter HAT-P-32b: clouds explain the absence of broad spectral features? , 436(4):2974–2988.
- Gibson, N. P., Aigrain, S., Pont, F., Sing, D. K., Désert, J. M., Evans, T. M., Henry, G., Husnoo, N., and Knutson, H. (2012). Probing the haze in the atmosphere of HD 189733b with Hubble Space Telescope/WFC3 transmission spectroscopy. , 422(1):753–760.
- Grillmair, C. J., Charbonneau, D., Burrows, A., Armus, L., Stauffer, J., Meadows, V., Van Cleve, J., and Levine, D. (2007). A Spitzer Spectrum of the Exoplanet HD 189733b. , 658(2):L115–L118.
- Grunblatt, S. K., Huber, D., Gaidos, E., Lopez, E. D., Howard, A. W., Isaacson, H. T., Sinukoff, E., Vanderburg, A., Nofi, L., Yu, J., North, T. S. H., Chaplin, W., Foreman-Mackey, D., Petigura, E., Ansdell, M., Weiss, L., Fulton, B., and Lin, D. N. C. (2017). Seeing Double with K2: Testing Re-inflation with Two Remarkably Similar Planets around Red Giant Branch Stars. , 154(6):254.
- Grunblatt, S. K., Huber, D., Gaidos, E. J., Lopez, E. D., Fulton, B. J., Vanderburg, A., Barclay, T., Fortney, J. J., Howard, A. W., Isaacson, H. T., Mann, A. W., Petigura, E., Silva Aguirre, V., and Sinukoff, E. J. (2016). K2-97b: A (Re-?)Inflated Planet Orbiting a Red Giant Star. , 152(6):185.
- Haight, F. A. (1967). *Handbook of the Poisson Distribution*.
- Haynes, K., Mandell, A. M., Madhusudhan, N., Deming, D., and Knutson, H. (2015). Spectroscopic Evidence for a Temperature Inversion in the Dayside Atmosphere of Hot Jupiter WASP-33b. , 806(2):146.
- Henry, G. W., Marcy, G. W., Butler, R. P., and Vogt, S. S. (2000). A Transiting “51 Peg-like” Planet. , 529(1):L41–L44.
- Hoeijmakers, H. J., Ehrenreich, D., Heng, K., Kitzmann, D., Grimm, S. L., Allart, R., Deitrick, R., Wyttenbach, A., Oreshenko, M., Pino, L., Rimmer, P. B., Molinari, E., and Di Fabrizio, L. (2018). Atomic iron and titanium in the atmosphere of the exoplanet KELT-9b. , 560(7719):453–455.
- Howard, A., Marcy, G., Johnson, J. A., Fischer, D., Wright, J., Valenti, J., Anderson, J., Lin, D. N. C., and Ida, S. (2011). The Occurrence And Mass Distribution Of Close-in Super-earths, Neptunes, And Jupiters. In *American Astronomical Society Meeting Abstracts #217*, volume 217 of *American Astronomical Society Meeting Abstracts*, page 415.06.
- Johnson, J. A., Aller, K. M., Howard, A. W., and Crepp, J. R. (2010). Giant Planet Occurrence in the Stellar Mass-Metallicity Plane. , 122(894):905.
- Jordán, A., Espinoza, N., Rabus, M., Eyheramendy, S., Sing, D. K., Désert, J.-M., Bakos, G. Á., Fortney, J. J., López-Morales, M., Maxted, P. F. L., Triaud, A. H. M. J., and Szentgyorgyi, A. (2013). A GROUND-BASED OPTICAL TRANSMISSION SPECTRUM OF WASP-6b. *The Astrophysical Journal*, 778(2):184.

- Kilpatrick, B. M., Cubillos, P. E., Stevenson, K. B., Lewis, N. K., Wakeford, H. R., MacDonald, R. J., Madhusudhan, N., Blecic, J., Bruno, G., Burrows, A., Deming, D., Heng, K., Line, M. R., Morley, C. V., Parmentier, V., Tucker, G. S., Valenti, J. A., Waldmann, I. P., Bean, J. L., Beichman, C., Fraine, J., Krick, J. E., Lothringer, J. D., and Mandell, A. M. (2018). Community Targets of JWST’s Early Release Science Program: Evaluation of WASP-63b. , 156(3):103.
- Kley, W. and Nelson, R. P. (2012). Planet-Disk Interaction and Orbital Evolution. , 50:211–249.
- Knutson, H. A., Charbonneau, D., Allen, L. E., Fortney, J. J., Agol, E., Cowan, N. B., Showman, A. P., Cooper, C. S., and Megeath, S. T. (2007a). A map of the day-night contrast of the extrasolar planet HD 189733b. , 447(7141):183–186.
- Knutson, H. A., Charbonneau, D., Burrows, A., O’Donovan, F. T., and Mandushev, G. (2009). Detection of A Temperature Inversion in the Broadband Infrared Emission Spectrum of TrES-4. , 691(1):866–874.
- Knutson, H. A., Charbonneau, D., Noyes, R. W., Brown, T. M., and Gilliland, R. L. (2007b). Using Stellar Limb-Darkening to Refine the Properties of HD 209458b. , 655(1):564–575.
- Komacek, T. D., Thorngren, D. P., Lopez, E. D., and Ginzburg, S. (2020). Re-inflation of Warm and Hot Jupiters. , 893(1):36.
- Kozai, Y. (1962). Secular perturbations of asteroids with high inclination and eccentricity. , 67:591–598.
- Kreidberg, L. (2015). batman: BAsic Transit Model cAlculatioN in Python. , 127(957):1161.
- Kreidberg, L., Bean, J. L., Désert, J.-M., Line, M. R., Fortney, J. J., Madhusudhan, N., Stevenson, K. B., Showman, A. P., Charbonneau, D., McCullough, P. R., Seager, S., Burrows, A., Henry, G. W., Williamson, M., Kataria, T., and Homeier, D. (2014). A Precise Water Abundance Measurement for the Hot Jupiter WASP-43b. , 793(2):L27.
- Le Verrier, U. J. (1846). Recherches sur les mouvements d’Uranus par U. J. Le Verrier (Fortsetzung). *Astronomische Nachrichten*, 25:65.
- Line, M. R. and Parmentier, V. (2016). THE INFLUENCE OF NONUNIFORM CLOUD COVER ON TRANSIT TRANSMISSION SPECTRA. *The Astrophysical Journal*, 820(1):78.
- Lopez, E. D. and Fortney, J. J. (2016). Re-inflated Warm Jupiters around Red Giants. , 818(1):4.
- MacDonald, R. J. and Madhusudhan, N. (2017). Signatures of Nitrogen Chemistry in Hot Jupiter Atmospheres. , 850(1):L15.
- Macintosh, B., Graham, J. R., Barman, T., De Rosa, R. J., Konopacky, Q., Marley, M. S., Marois, C., Nielsen, E. L., Pueyo, L., Rajan, A., Rameau, J., Saumon, D., Wang, J. J., Patience, J., Ammons, M., Arriaga, P., Artigau, E., Beckwith, S., Brewster, J., Bruzzone, S., Bulger, J., Burningham, B., Burrows, A. S., Chen, C., Chiang, E., Chilcote, J. K., Dawson, R. I., Dong, R., Doyon, R., Draper, Z. H., Duchêne, G., Esposito, T. M., Fabrycky, D., Fitzgerald, M. P., Follette, K. B., Fortney, J. J., Gerard, B., Goodsell, S., Greenbaum, A. Z., Hibon, P., Hinkley, S., Cotten, T. H., Hung, L. W., Ingraham, P., Johnson-Groh, M., Kalas, P., Lafreniere, D., Larkin, J. E., Lee, J., Line, M., Long, D., Maire, J., Marchis, F., Matthews, B. C., Max, C. E., Metchev, S., Millar-Blanchaer, M. A., Mittal, T., Morley, C. V., Morzinski, K. M., Murray-Clay, R., Oppenheimer, R., Palmer, D. W., Patel, R., Perrin, M. D., Poyneer, L. A., Rafikov, R. R., Rantakyrö, F. T., Rice, E. L., Rojo, P., Rudy, A. R., Ruffio, J. B., Ruiz, M. T., Sadakuni, N., Saddlemyer, L., Salama, M., Savransky, D., Schneider, A. C., Sivaramakrishnan, A., Song, I., Soummer, R., Thomas, S., Vasisht, G., Wallace, J. K., Ward-Duong, K., Wiktorowicz, S. J., Wolff, S. G., and Zuckerman, B. (2015). Discovery and spectroscopy of the young jovian planet 51 Eri b with the Gemini Planet Imager. *Science*, 350(6256):64–67.
- Madhusudhan, N. (2012). C/O Ratio as a Dimension for Characterizing Exoplanetary Atmospheres. , 758(1):36.
- Madhusudhan, N. (2019). Exoplanetary Atmospheres: Key Insights, Challenges, and Prospects. , 57:617–663.
- Madhusudhan, N., Amin, M. A., and Kennedy, G. M. (2014). Toward Chemical Constraints on Hot Jupiter Migration. , 794(1):L12.
- Mallonn, M., von Essen, C., Weingrill, J., Strassmeier, K. G., Ribas, I., Carroll, T. A., Herrero, E., Granzer, T., Claret, A., and Schwöpe, A. (2015). Transmission spectroscopy of the inflated exo-Saturn HAT-P-19b. , 580:A60.
- Mandel, K. and Agol, E. (2002). Analytic Light Curves for Planetary Transit Searches. , 580(2):L171–L175.

- Mao, S. and Paczynski, B. (1991). Gravitational Microlensing by Double Stars and Planetary Systems. , 374:L37.
- Mayor, M., Marmier, M., Lovis, C., Udry, S., Ségransan, D., Pepe, F., Benz, W., Bertaux, J. L., Bouchy, F., Dumusque, X., Lo Curto, G., Mordasini, C., Queloz, D., and Santos, N. C. (2011). The HARPS search for southern extra-solar planets XXXIV. Occurrence, mass distribution and orbital properties of super-Earths and Neptune-mass planets. *arXiv e-prints*, page arXiv:1109.2497.
- Mayor, M. and Queloz, D. (1995). A Jupiter-mass companion to a solar-type star. , 378(6555):355–359.
- Mazeh, T., Holczer, T., and Faigler, S. (2016). Dearth of short-period Neptunian exoplanets: A desert in period-mass and period-radius planes. , 589:A75.
- Mazeh, T., Naef, D., Torres, G., Latham, D. W., Mayor, M., Beuzit, J.-L., Brown, T. M., Buchhave, L., Burnet, M., Carney, B. W., Charbonneau, D., Druker, G. A., Laird, J. B., Pepe, F., Perrier, C., Queloz, D., Santos, N. C., Sivan, J.-P., Udry, S., and Zucker, S. (2000). The Spectroscopic Orbit of the Planetary Companion Transiting HD 209458. , 532(1):L55–L58.
- McCullough, P. R., Stys, J. E., Valenti, J. A., Fleming, S. W., Janes, K. A., and Heasley, J. N. (2005). The XO Project: Searching for Transiting Extrasolar Planet Candidates. , 117(834):783–795.
- McLaughlin, D. B. (1924). Some results of a spectrographic study of the Algol system. , 60:22–31.
- Miller, N. and Fortney, J. J. (2011). The Heavy-element Masses of Extrasolar Giant Planets, Revealed. , 736(2):L29.
- Moses, J. I., Madhusudhan, N., Visscher, C., and Freedman, R. S. (2013). Chemical Consequences of the C/O Ratio on Hot Jupiters: Examples from WASP-12b, CoRoT-2b, XO-1b, and HD 189733b. , 763(1):25.
- Moses, J. I., Visscher, C., Fortney, J. J., Showman, A. P., Lewis, N. K., Griffith, C. A., Klippenstein, S. J., Shabram, M., Friedson, A. J., Marley, M. S., and Freedman, R. S. (2011). Disequilibrium Carbon, Oxygen, and Nitrogen Chemistry in the Atmospheres of HD 189733b and HD 209458b. , 737(1):15.
- Nascimbeni, V., Piotto, G., Pagano, I., Scandariato, G., Sani, E., and Fumana, M. (2013). The blue sky of GJ3470b: the atmosphere of a low-mass planet unveiled by ground-based photometry. , 559:A32.
- Nielsen, E., De Rosa, R., Macintosh, B., Wang, J., Ruffio, J.-B., Chiang, E., Marley, M., Saumon, D., Savransky, D., Fabrycky, D., Konopacky, Q., Patience, J., and Bailey, V. (2019a). The Gemini Planet Imager Exoplanet Survey: Giant Planet and Brown Dwarf Demographics from 10-100 AU. In *AAS/Division for Extreme Solar Systems Abstracts*, volume 51 of *AAS/Division for Extreme Solar Systems Abstracts*, page 100.02.
- Nielsen, E. L., De Rosa, R. J., Macintosh, B., Wang, J. J., Ruffio, J.-B., Chiang, E., Marley, M. S., Saumon, D., Savransky, D., Ammons, S. M., Bailey, V. P., Barman, T., Blain, C., Bulger, J., Burrows, A., Chilcote, J., Cotten, T., Czekala, I., Doyon, R., Duchêne, G., Esposito, T. M., Fabrycky, D., Fitzgerald, M. P., Follette, K. B., Fortney, J. J., Gerard, B. L., Goodsell, S. J., Graham, J. R., Greenbaum, A. Z., Hibon, P., Hinkley, S., Hirsch, L. A., Hom, J., Hung, L.-W., Dawson, R. I., Ingraham, P., Kalas, P., Konopacky, Q., Larkin, J. E., Lee, E. J., Lin, J. W., Maire, J., Marchis, F., Marois, C., Metchev, S., Millar-Blanchaer, M. A., Morzinski, K. M., Oppenheimer, R., Palmer, D., Patience, J., Perrin, M., Poyneer, L., Pueyo, L., Rafikov, R. R., Rajan, A., Rameau, J., Rantakyro, F. T., Ren, B., Schneider, A. C., Sivaramakrishnan, A., Song, I., Soummer, R., Tallis, M., Thomas, S., Ward-Duong, K., and Wolff, S. (2019b). The Gemini Planet Imager Exoplanet Survey: Giant Planet and Brown Dwarf Demographics from 10 to 100 au. , 158(1):13.
- Nielsen, E. L., Liu, M. C., Wahhaj, Z., Biller, B. A., Hayward, T. L., Close, L. M., Males, J. R., Skemer, A. J., Chun, M., Ftacelas, C., Alencar, S. H. P., Artymowicz, P., Boss, A., Clarke, F., de Gouveia Dal Pino, E., Gregorio-Hetem, J., Hartung, M., Ida, S., Kuchner, M., Lin, D. N. C., Reid, I. N., Shkolnik, E. L., Tecza, M., Thatte, N., and Toomey, D. W. (2013). The Gemini NICI Planet-Finding Campaign: The Frequency of Giant Planets around Young B and A Stars. , 776(1):4.
- Nikolov, N., Sing, D. K., Burrows, A. S., Fortney, J. J., Henry, G. W., Pont, F., Ballester, G. E., Aigrain, S., Wilson, P. A., Huitson, C. M., Gibson, N. P., Désert, J. M., Lecavelier Des Etangs, A., Showman, A. P., Vidal-Madjar, A., Wakeford, H. R., and Zahnle, K. (2015). HST hot-Jupiter transmission spectral survey: haze in the atmosphere of WASP-6b. , 447(1):463–478.
- Öberg, K. I., Murray-Clay, R., and Bergin, E. A. (2011). The Effects of Snowlines on C/O in Planetary Atmospheres. , 743(1):L16.

- Oshagh, M., Santos, N. C., Ehrenreich, D., Haghhighipour, N., Figueira, P., Santerne, A., and Montalto, M. (2014). Impact of occultations of stellar active regions on transmission spectra. Can occultation of a plage mimic the signature of a blue sky? , 568:A99.
- Parmentier, V., Line, M. R., Bean, J. L., Mansfield, M., Kreidberg, L., Lupu, R., Visscher, C., Désert, J.-M., Fortney, J. J., Deleuil, M., Arcangeli, J., Showman, A. P., and Marley, M. S. (2018). From thermal dissociation to condensation in the atmospheres of ultra hot Jupiters: WASP-121b in context. , 617:A110.
- Pepper, J., Stassun, K. G., and Gaudi, B. S. (2018). *KELT: The Kilodegree Extremely Little Telescope, a Survey for Exoplanets Transiting Bright, Hot Stars*, page 128.
- Petigura, E. A., Marcy, G. W., Winn, J. N., Weiss, L. M., Fulton, B. J., Howard, A. W., Sinukoff, E., Isaacson, H., Morton, T. D., and Johnson, J. A. (2018). The California-Kepler Survey. IV. Metal-rich Stars Host a Greater Diversity of Planets. , 155(2):89.
- Petrovich, C. (2015). Hot Jupiters from Coplanar High-eccentricity Migration. , 805(1):75.
- Petrovich, C., Tremaine, S., and Rafikov, R. (2014). Scattering Outcomes of Close-in Planets: Constraints on Planet Migration. , 786(2):101.
- Pierce, A. K. and Slaughter, C. D. (1977). Solar limb darkening. I:  $\lambda\lambda$  (3033 - 7297). , 51(1):25–41.
- Piso, A.-M. A., Öberg, K. I., Birnstiel, T., and Murray-Clay, R. A. (2015). C/O and Snowline Locations in Protoplanetary Disks: The Effect of Radial Drift and Viscous Gas Accretion. , 815(2):109.
- Pont, F., Gilliland, R. L., Moutou, C., Charbonneau, D., Bouchy, F., Brown, T. M., Mayor, M., Queloz, D., Santos, N., and Udry, S. (2007). Hubble Space Telescope time-series photometry of the planetary transit of HD 189733: no moon, no rings, starspots. , 476(3):1347–1355.
- Pont, F., Knutson, H., Gilliland, R. L., Moutou, C., and Charbonneau, D. (2008). Detection of atmospheric haze on an extrasolar planet: the 0.55-1.05  $\mu\text{m}$  transmission spectrum of HD 189733b with the HubbleSpaceTelescope. , 385(1):109–118.
- Pont, F., Sing, D. K., Gibson, N. P., Aigrain, S., Henry, G., and Husnoo, N. (2013). The prevalence of dust on the exoplanet HD 189733b from Hubble and Spitzer observations. , 432(4):2917–2944.
- Rafikov, R. R. (2005). Can Giant Planets Form by Direct Gravitational Instability? , 621(1):L69–L72.
- Rasio, F. A. and Ford, E. B. (1996). Dynamical instabilities and the formation of extrasolar planetary systems. *Science*, 274:954–956.
- Richardson, L. J., Deming, D., Horning, K., Seager, S., and Harrington, J. (2007). A spectrum of an extrasolar planet. , 445(7130):892–895.
- Ricker, G. R., Winn, J. N., Vanderspek, R., Latham, D. W., Bakos, G. Á., Bean, J. L., Berta-Thompson, Z. K., Brown, T. M., Buchhave, L., Butler, N. R., Butler, R. P., Chaplin, W. J., Charbonneau, D., Christensen-Dalsgaard, J., Clampin, M., Deming, D., Doty, J., De Lee, N., Dressing, C., Dunham, E. W., Endl, M., Fressin, F., Ge, J., Henning, T., Holman, M. J., Howard, A. W., Ida, S., Jenkins, J., Jernigan, G., Johnson, J. A., Kaltenegger, L., Kawai, N., Kjeldsen, H., Laughlin, G., Levine, A. M., Lin, D., Lissauer, J. J., MacQueen, P., Marcy, G., McCullough, P. R., Morton, T. D., Narita, N., Paegert, M., Palle, E., Pepe, F., Pepper, J., Quirrenbach, A., Rinehart, S. A., Sasselov, D., Sato, B., Seager, S., Sozzetti, A., Stassun, K. G., Sullivan, P., Szentgyorgyi, A., Torres, G., Udry, S., and Villaseñor, J. (2014). Transiting Exoplanet Survey Satellite (TESS). In Oschmann, Jacobus M., J., Clampin, M., Fazio, G. G., and MacEwen, H. A., editors, *Space Telescopes and Instrumentation 2014: Optical, Infrared, and Millimeter Wave*, volume 9143 of *Society of Photo-Optical Instrumentation Engineers (SPIE) Conference Series*, page 914320.
- Rossiter, R. A. (1924). On the detection of an effect of rotation during eclipse in the velocity of the brighter component of beta Lyrae, and on the constancy of velocity of this system. , 60:15–21.
- Shallue, C. J. and Vanderburg, A. (2018). Identifying Exoplanets with Deep Learning: A Five-planet Resonant Chain around Kepler-80 and an Eighth Planet around Kepler-90. , 155(2):94.
- Sheppard, K. B., Mandell, A. M., Tamburo, P., Gandhi, S., Pinhas, A., Madhusudhan, N., and Deming, D. (2017). Evidence for a Dayside Thermal Inversion and High Metallicity for the Hot Jupiter WASP-18b. , 850(2):L32.
- Showman, A. P. and Guillot, T. (2002). Atmospheric circulation and tides of “51 Pegasus b-like” planets. , 385:166–180.

- Sing, D. K. (2010). VizieR Online Data Catalog: Stellar Limb-Darkening Coefficients (Sing, 2010). *VizieR Online Data Catalog*, pages J/A+A/510/A21.
- Sing, D. K., Désert, J. M., Fortney, J. J., Lecavelier Des Etangs, A., Ballester, G. E., Cepa, J., Ehrenreich, D., López-Morales, M., Pont, F., Shabram, M., and Vidal-Madjar, A. (2011a). Gran Telescopio Canarias OSIRIS transiting exoplanet atmospheric survey: detection of potassium in XO-2b from narrowband spectrophotometry. , 527:A73.
- Sing, D. K., Fortney, J. J., Nikolov, N., Wakeford, H. R., Kataria, T., Evans, T. M., Aigrain, S., Ballester, G. E., Burrows, A. S., Deming, D., Désert, J.-M., Gibson, N. P., Henry, G. W., Huitson, C. M., Knutson, H. A., Lecavelier Des Etangs, A., Pont, F., Showman, A. P., Vidal-Madjar, A., Williamson, M. H., and Wilson, P. A. (2016). A continuum from clear to cloudy hot-Jupiter exoplanets without primordial water depletion. , 529(7584):59–62.
- Sing, D. K., Lecavelier des Etangs, A., Fortney, J. J., Burrows, A. S., Pont, F., Wakeford, H. R., Ballester, G. E., Nikolov, N., Henry, G. W., Aigrain, S., Deming, D., Evans, T. M., Gibson, N. P., Huitson, C. M., Knutson, H., Showman, A. P., Vidal-Madjar, A., Wilson, P. A., Williamson, M. H., and Zahnle, K. (2013). HST hot-Jupiter transmission spectral survey: evidence for aerosols and lack of TiO in the atmosphere of WASP-12b. , 436(4):2956–2973.
- Sing, D. K., Pont, F., Aigrain, S., Charbonneau, D., Désert, J. M., Gibson, N., Gilliland, R., Hayek, W., Henry, G., Knutson, H., Lecavelier Des Etangs, A., Mazeh, T., and Shporer, A. (2011b). Hubble Space Telescope transmission spectroscopy of the exoplanet HD 189733b: high-altitude atmospheric haze in the optical and near-ultraviolet with STIS. , 416(2):1443–1455.
- Sing, D. K., Vidal-Madjar, A., Désert, J. M., Lecavelier des Etangs, A., and Ballester, G. (2008). Hubble Space Telescope STIS Optical Transit Transmission Spectra of the Hot Jupiter HD 209458b. , 686(1):658–666.
- Sing, D. K., Wakeford, H. R., Showman, A. P., Nikolov, N., Fortney, J. J., Burrows, A. S., Ballester, G. E., Deming, D., Aigrain, S., Désert, J. M., Gibson, N. P., Henry, G. W., Knutson, H., Lecavelier des Etangs, A., Pont, F., Vidal-Madjar, A., Williamson, M. W., and Wilson, P. A. (2015). HST hot-Jupiter transmission spectral survey: detection of potassium in WASP-31b along with a cloud deck and Rayleigh scattering. , 446(3):2428–2443.
- Snellen, I. A. G., de Kok, R. J., de Mooij, E. J. W., and Albrecht, S. (2010). The orbital motion, absolute mass and high-altitude winds of exoplanet HD209458b. , 465(7301):1049–1051.
- Spake, J. J., Sing, D. K., Evans, T. M., Oklopčić, A., Bourrier, V., Kreidberg, L., Rackham, B. V., Irwin, J., Ehrenreich, D., Wyttenbach, A., Wakeford, H. R., Zhou, Y., Chubb, K. L., Nikolov, N., Goyal, J. M., Henry, G. W., Williamson, M. H., Blumenthal, S., Anderson, D. R., Hellier, C., Charbonneau, D., Udry, S., and Madhusudhan, N. (2018). Helium in the eroding atmosphere of an exoplanet. , 557(7703):68–70.
- Stefansson, G., Mahadevan, S., Hebb, L., Wisniewski, J., Huehnerhoff, J., Morris, B., Halverson, S., Zhao, M., Wright, J., O’rouke, J., Knutson, H., Hawley, S., Kanodia, S., Li, Y., Hagen, L. M. Z., Liu, L. J., Beatty, T., Bender, C., Robertson, P., Dembicky, J., Gray, C., Ketzebach, W., McMillan, R., and Rudyk, T. (2017). Toward Space-like Photometric Precision from the Ground with Beam-shaping Diffusers. , 848(1):9.
- Stevenson, K. B., Désert, J.-M., Line, M. R., Bean, J. L., Fortney, J. J., Showman, A. P., Kataria, T., Kreidberg, L., McCullough, P. R., Henry, G. W., Charbonneau, D., Burrows, A., Seager, S., Madhusudhan, N., Williamson, M. H., and Homeier, D. (2014). Thermal structure of an exoplanet atmosphere from phase-resolved emission spectroscopy. *Science*, 346(6211):838–841.
- Stevenson, K. B., Line, M. R., Bean, J. L., Désert, J.-M., Fortney, J. J., Showman, A. P., Kataria, T., Kreidberg, L., and Feng, Y. K. (2017). Spitzer Phase Curve Constraints for WASP-43b at 3.6 and 4.5  $\mu\text{m}$ . , 153(2):68.
- Street, R. A., Pollaco, D. L., Fitzsimmons, A., Keenan, F. P., Horne, K., Kane, S., Collier Cameron, A., Lister, T. A., Haswell, C., Norton, A. J., Jones, B. W., Skillen, I., Hodgkin, S., Wheatley, P., West, R., and Brett, D. (2003). SuperWASP: Wide Angle Search for Planets. In Deming, D. and Seager, S., editors, *Scientific Frontiers in Research on Extrasolar Planets*, volume 294 of *Astronomical Society of the Pacific Conference Series*, pages 405–408.
- Tsiaras, A., Waldmann, I. P., Zingales, T., Rocchetto, M., Morello, G., Damiano, M., Karpouzas, K., Tinetti, G., McKemmish, L. K., Tennyson, J., and Yurchenko, S. N. (2018). A Population Study of Gaseous Exoplanets. , 155(4):156.

- Udalski, A., Szymanski, M., Kaluzny, J., Kubiak, M., and Mateo, M. (1992). The Optical Gravitational Lensing Experiment. , 42:253–284.
- Vidal-Madjar, A., Désert, J. M., Lecavelier des Etangs, A., Hébrard, G., Ballester, G. E., Ehrenreich, D., Ferlet, R., McConnell, J. C., Mayor, M., and Parkinson, C. D. (2004). Detection of Oxygen and Carbon in the Hydrodynamically Escaping Atmosphere of the Extrasolar Planet HD 209458b. , 604(1):L69–L72.
- Vidal-Madjar, A., Lecavelier des Etangs, A., Désert, J. M., Ballester, G. E., Ferlet, R., Hébrard, G., and Mayor, M. (2003). An extended upper atmosphere around the extrasolar planet HD209458b. , 422(6928):143–146.
- Vigan, A., Fontanive, C., Meyer, M., Biller, B., Bonavita, M., Feldt, M., Desidera, S., Marleau, G. D., Emsenhuber, A., Galicher, R., Rice, K., Forgan, D., Mordasini, C., Gratton, R., Le Coroller, H., Maire, A. L., Cantalloube, F., Chauvin, G., Cheetham, A., Hagelberg, J., Lagrange, A. M., Langlois, M., Bonnefoy, M., Beuzit, J. L., Boccaletti, A., D’Orazi, V., Delorme, P., Dominik, C., Henning, T., Janson, M., Lagadec, E., Lazzoni, C., Ligi, R., Menard, F., Mesa, D., Messina, S., Moutou, C., Müller, A., Perrot, C., Samland, M., Schmid, H. M., Schmidt, T., Sissa, E., Turatto, M., Udry, S., Zurlo, A., Abe, L., Antichi, J., Asensio-Torres, R., Baruffolo, A., Baudoz, P., Baudrand, J., Bazzon, A., Blanchard, P., Bohn, A. J., Brown Sevilla, S., Carbillat, M., Carle, M., Cascone, E., Charton, J., Claudi, R., Costille, A., De Caprio, V., Delboulb e, A., Dohlen, K., Engler, N., Fantinel, D., Feautrier, P., Fusco, T., Gigan, P., Girard, J. H., Giro, E., Gisler, D., Gluck, L., Gry, C., Hubin, N., Hugot, E., Jaquet, M., Kasper, M., Le Mignant, D., Llored, M., Madec, F., Magnard, Y., Martinez, P., Maurel, D., M oller-Nilsson, O., Mouillet, D., Moulin, T., Orign e, A., Pavlov, A., Perret, D., Petit, C., Pragt, J., Puget, P., Rabou, P., Ramos, J., Rickman, E. L., Rigal, F., Rochat, S., Roelfsema, R., Rousset, G., Roux, A., Salasnich, B., Sauvage, J. F., Sevin, A., Soenke, C., Stadler, E., Suarez, M., Wahhaj, Z., Weber, L., and Wildi, F. (2020). The SPHERE infrared survey for exoplanets (SHINE). III. The demographics of young giant exoplanets below 300 au with SPHERE. *arXiv e-prints*, page arXiv:2007.06573.
- Weiss, L. M., Marcy, G. W., Petigura, E. A., Fulton, B. J., Howard, A. W., Winn, J. N., Isaacson, H. T., Morton, T. D., Hirsch, L. A., Sinukoff, E. J., Cumming, A., Hebb, L., and Cargile, P. A. (2018). The California-Kepler Survey. V. Peas in a Pod: Planets in a Kepler Multi-planet System Are Similar in Size and Regularly Spaced. , 155(1):48.
- West, R. G., Gillen, E., Bayliss, D., Burleigh, M. R., Delrez, L., G unther, M. N., Hodgkin, S. T., Jackman, J. A. G., Jenkins, J. S., King, G., McCormac, J., Nielsen, L. D., Raynard, L., Smith, A. M. S., Soto, M., Turner, O., Wheatley, P. J., Almlaeky, Y., Armstrong, D. J., Belardi, C., Bouchy, F., Briegal, J. T., Burdanov, A., Cabrera, J., Casewell, S. L., Chaushev, A., Chazelas, B., Chote, P., Cooke, B. F., Csizmadia, S., Ducrot, E., Eigm uller, P., Erikson, A., Foxell, E., G ansicke, B. T., Gillon, M., Goad, M. R., Jehin, E., Lambert, G., Longstaff, E. S., Loudon, T., Moyano, M., Murray, C., Pollacco, D., Queloz, D., Rauer, H., Sohy, S., Thompson, S. J., Udry, S., Walker, S. R., and Watson, C. A. (2019). NGTS-4b: A sub-Neptune transiting in the desert. , 486(4):5094–5103.
- West, R. G., Pollacco, D., Wheatley, P., Goad, M., Queloz, D., Rauer, H., Watson, C., Udry, S., Bannister, N., Bayliss, D., Bouchy, F., Burleigh, M., Cabrera, J., Chaushev, A., Chazelas, B., Crausaz, M., Csizmadia, S., Eigm uller, P., Erikson, A., Genolet, L., Gillen, E., Grange, A., G unther, M., Hodgkin, S., Kirk, J., Lambert, G., Loudon, T., McCormac, J., Metrailler, L., Neveu, M., Smith, A., Thompson, A., Raddi, R., Walker, S. R., Jenkins, J., and Jord an, A. (2016). The Next Generation Transit Survey Becomes Operational at Paranal. *The Messenger*, 165:10–12.
- Winn, J. N. (2014). Transits and occultations.
- Wolszczan, A. and Frail, D. A. (1992). A planetary system around the millisecond pulsar PSR1257 + 12. , 355(6356):145–147.
- Wolter, U., Schmitt, J. H. M. M., Huber, K. F., Czesla, S., M uller, H. M., Guenther, E. W., and Hatzes, A. P. (2009). Transit mapping of a starspot on CoRoT-2. Probing a stellar surface with planetary transits. , 504(2):561–564.
- Wytenbach, A., Ehrenreich, D., Lovis, C., Udry, S., and Pepe, F. (2015). Spectrally resolved detection of sodium in the atmosphere of HD 189733b with the HARPS spectrograph. , 577:A62.
- Zhang, M., Knutson, H. A., Kataria, T., Schwartz, J. C., Cowan, N. B., Showman, A. P., Burrows, A., Fortney, J. J., Todorov, K., Desert, J.-M., Agol, E., and Deming, D. (2018). Phase Curves of WASP-33b and HD 149026b and a New Correlation between Phase Curve Offset and Irradiation Temperature. , 155(2):83.